Quarterly Technical Report

Solid State Research

1992:1

Lincoln Laboratory

MASSACHUSETTS INSTITUTE OF TECHNOLOGY

LEXINGTON, MASSACHUSETTS

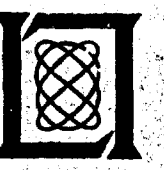

Prepared for the Department of the Air Force under Contract F19628-90-C-0002.

This report is based on studies performed at Lincoln Laboratory, a center for research operated by Massachusetts Institute of Technology. The work was sponsored by the Department of the Air Force under Contract F19628-90-C-0002.

The ESC Public Affairs Office has reviewed this report, and it is releasable to the National Technical Information Service, where it will be available to the general public, including foreign nationals.

This technical report has been reviewed and is approved for publication.

FOR THE COMMANDER

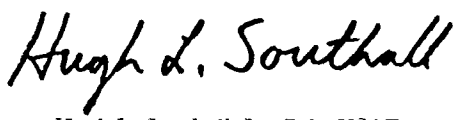

Hugh L. Southall, Lt. Col., USAF
Chief, ESC Lincoln Laboratory Project Office

Non-Lincoln Recipients

PLEASE DO NOT RETURN

Permission is given to destroy this document when it is no longer needed.

MASSACHUSETTS INSTITUTE OF TECHNOLOGY
LINCOLN LABORATORY

SOLID STATE RESEARCH

QUARTERLY TECHNICAL REPORT

1 NOVEMBER 1991 — 31 JANUARY 1992

ISSUED 31 JULY 1992

ABSTRACT

This report covers in detail the research work of the Solid State Division at Lincoln Laboratory for the period 1 November 1991 through 31 January 1992. The topics covered are Electrooptical Devices, Quantum Electronics, Materials Research, Submicrometer Technology, High Speed Electronics, Microelectronics, and Analog Device Technology. Funding is provided primarily by the Air Force, with additional support provided by the Army, DARPA, Navy, SDIO, NASA, and DOE.

TABLE OF CONTENTS

LIST OF ILLUSTRATIONS

LIST OF ILLUSTRATIONS (Continued)

LIST OF ILLUSTRATIONS (Continued)

LIST OF TABLES

INTRODUCTION

1. ELECTROOPTICAL DEVICES

An analytical model has been developed for the effect of incomplete smoothing in mass-transported microlenses. The knowledge of acceptable residual ripples that is obtained can result in practical time-saving measures in the fabrication of large-aperture microlenses.

Signal cancellation measurements have been performed on integrated-optical modulators being developed for an adaptive nulling system. Cancellation of ~ 36 dB has been obtained over the frequency band 5 to 7 GHz.

Aluminum-free, strained-layer quantum-well lasers have been fabricated with a GaInAsP quaternary alloy as the optical-confinement-layer material. These devices, which have deeper quantum wells than earlier aluminum-free devices with GaAs confinement layers, exhibit differential quantum efficiencies > 40%/facet.

2. QUANTUM ELECTRONICS

An analytic solution has been obtained for the stress-induced birefringence in a Nd:YAG disk when the thermal distribution is Gaussian. For uniform illumination of the disk, the round-trip loss due to the stress-induced birefringence and an intracavity polarizer is calculated numerically and compared with the case for uniform heat distribution within the disk.

3. MATERIALS RESEARCH

The first GaInAsSb/AlGaAsSb diode lasers with a quantum-well active region have been demonstrated. These devices, which emit at 2.1 μm, show a dramatic improvement in performance over double-heterostructure GaInAsSb/AlGaAsSb lasers, with continuous output power up to 190 A/cm^2 for operation at a heatsink temperature of 20°C.

The sensitivity of infrared focal plane arrays (FPAs) utilizing Si-based detectors has been increased by using monolithic microlens arrays to increase the detector fill factor. Each microlens, which is fabricated directly on the back side of the FPA Si wafer in registration with an individual pixel, serves as a reimaging field lens between the primary objective lens and the FPA to refocus the incident radiation onto the detector.

In growth interruption experiments performed to investigate the potential of in situ CH_3I etching technology, organometallic vapor phase epitaxy has been used to grow a second GaAs epilayer on first epilayers that were either untreated or etched in a separate reactor with CH_3I vapor and/or H_2SO_4. For CH_3I etch temperatures below 500°C, the surface morphology and low-temperature photoluminescence are comparable for epilayers grown on CH_3I-etched and untreated first epilayers, while carrier concentration depth profiles show that CH_3I etching not only introduces very little electron accumulation at the regrowth interface but also eliminates most of the electron accumulation resulting from H_2SO_4 etching.

4. SUBMICROMETER TECHNOLOGY

An AlGaAs surface-emitting semiconductor laser, grown by molecular beam epitaxy and incorporating a circularly symmetric grating of period $\Lambda = 0.25$ μm, has been fabricated using electron-beam lithography. Azimuthal variations in the grating linewidth are shown to have a significant impact on the spatial modes of the laser.

An all-dry technique has been developed for selective-area growth of SiO_2 films induced by excimer laser photolysis. Patterning of 0.5-μm features has been achieved, and pattern transfer using oxygen reactive ion etching has been demonstrated.

5. HIGH SPEED ELECTRONICS

A new type of power GaAs permeable base transistor (PBT) has been fabricated that uses a monolithic multicell design. The dc and RF performance of these devices scales well from that of earlier single-cell PBTs.

Data from computer-aided active load-pull measurements of multicell PBTs have been used to design high-efficiency 20-GHz power amplifiers. Fabricated amplifiers have demonstrated an output power of 430 mW with a power-added efficiency of 33%.

6. MICROELECTRONICS

A charge-coupled device (CCD) architecture for implementing radix-4 fast Fourier transforms (FFTs) has been developed. Based on an error analysis and computer simulation of the effects of weight truncation and round-off error in computation, a 1024-point FFT in which each output is accurate to approximately 6 bits can be obtained using intermediate computations accurate to 8 bits.

7. ANALOG DEVICE TECHNOLOGY

A flexible, analog-ternary (plus, minus, and zero reference weights) dual-correlator chip has been designed and fabricated using a custom 2-μm CMOS/CCD process. The two identical and independent correlator subunits have programmable lengths of up to 512 samples and can operate at up to 50-MHz sample rates.

A gas conduction heater has been demonstrated that is capable of heating a 2-in.-diam $LaAlO_3$ substrate to 720°C with a temperature difference over the substrate area of < 1°C. This heater has been used to deposit uniform YBCO superconductive films.

REPORTS ON SOLID STATE RESEARCH

1 NOVEMBER 1991 THROUGH 31 JANUARY 1992

PUBLICATIONS

Resonant Tunneling in High-Speed Double-Barrier Diodes	E. R. Brown	In *Hot Carriers in Semiconductor Microstructures* (Academic, Orlando, Florida, 1992), pp. 469-498
GaAs-Based Diode Lasers on Si with Increased Lifetime Obtained by Using Strained InGaAs Active Layer	H. K. Choi C. A. Wang N. H. Karam*	*Appl. Phys. Lett.* **59**, 2634 (1991)
Piezoelectric Micromotors for Microrobots	A. M. Flynn* L. S. Tavrow* S. F. Bart* R. A. Brooks* D. J. Ehrlich K. R. Udayakumar* L. E. Cross*	*IEEE J. Microelectromech. Syst.* **1**, 44 (1992)
Electrical and Structural Characterization of GaAs Vertical-Sidewall Epilayers Grown by Atomic Layer Epitaxy	D. B. Gladden W. D. Goodhue C. A. Wang	*J. Electron. Mater.* **21**, 109 (1992)
Surface Imaging Lithography	M. A. Hartney	*OSA Proceedings on Soft-X-Ray Projection Lithography*, Vol. 12, J. Bokor, ed. (Optical Society of America, Washington, D.C., 1991), p. 120
Surface Imaging of Focused Ion-Beam Exposed Resists	M. A. Hartney D. C. Shaver M. I. Shepard* J. Melngailis* V. Medvedev* W. P. Robinson*	*J. Vac. Sci. Technol. B* **9**, 3432 (1991)

*Author not at Lincoln Laboratory.

Antireflection Layers and Planarization for Microlithography	M. W. Horn	*Solid State Technol.* **34**(11), 57 (1991)
Sub-μm, Planarized, Nb-AlO_x-Nb Josephson Process for 125 mm Wafers Developed in Partnership with Si Technology	M. B. Ketchen* D. Pearson* A. W. Kleinsasser* C.-K. Hu* M. Smyth* J. Logan* K. Stawiasz* E. Baran* M. Jaso* T. Ross* K. Petrillo* M. Manny* S. Basavaiah* S. Brodsky* S. B. Kaplan* W. J. Gallagher* M. Bhushan	*Appl. Phys. Lett.* **59**, 2609 (1991)
Continuous-Wave Operation of a Diode-Pumped Rotating Nd:Glass Disk Laser	J. Korn T. H. Jeys T. Y. Fan	*Opt. Lett.* **16**, 1741 (1991)
Dry-Developed Organosilicon Resists for 193-nm Excimer Laser Lithography	R. R. Kunz M. W. Horn	*Conference Preprints of the 9th Regional (Mid-Hudson Section) Technical Conference on Photopolymers* (Society of Plastics Engineers, Brookfield, Connecticut, 1991), p. 291
Low-Threshold InGaAs Strained-Layer Quantum-Well Lasers ($\lambda = 0.98$ μm) with GaInP Cladding Layers and Mass-Transported Buried Heterostructure	Z. L. Liau S. C. Palmateer S. H. Groves J. N. Walpole L. J. Missaggia	*Appl. Phys. Lett.* **60**, 6 (1992)

*Author not at Lincoln Laboratory.

High-Frequency Analog Signal Processing with High-Temperature Superconductors	W. G. Lyons R. S. Withers J. M. Hamm R. H. Mathews B. J. Clifton P. M. Mankiewich* M. L. O'Malley* N. Newman*	*OSA Proceedings on Picosecond Electronics and Optoelectronics*, Vol. 9, T. C. L. G. Sollner and J. Shah, eds. (Optical Society of America, Washington, D.C., 1991), p. 167
Ultraviolet Photoresponse Characteristics of Diamond Diodes	M. Marchywka* J. F. Hochedez* M. W. Geis D. G. Socker* D. Moses* R. T. Goldberg*	*Appl. Opt.* **30**, 5011 (1991)
Increase in Silicon Charge Coupled Devices Speed with Focused Ion Beam Implanted Channels	J. E. Murguia* M. I. Shepard* J. Melngailis* A. L. Lattes S. C. Munroe	*J. Vac. Sci. Technol. B* **9**, 2714 (1991)
Terahertz Time-Domain Measurement of the Conductivity and Superconducting Band Gap in Niobium	M. C. Nuss* K. W. Goossen* J. P. Gordon* P. M. Mankiewich* M. L. O'Malley* M. Bhushan	*J. Appl. Phys.* **70**, 2238 (1991)
Terahertz Time-Domain Transmission of Superconductors	M. C. Nuss* P. M. Mankiewich* M. O'Malley* K. W. Goossen* H. Roskos* B. Tell* M. Bhushan	*OSA Proceedings on Picosecond Electronics and Optoelectronics*, Vol. 9, T. C. L. G. Sollner and J. Shah, eds. (Optical Society of America, Washington, D.C., 1991), p. 31

*Author not at Lincoln Laboratory.

Microwave Applications of Superconducting Electronics	R. W. Ralston	*Supercond. Sci. Technol.* **4**, 386 (1991)
Laser-Induced Metal Deposition and Laser Cutting Techniques for Fixing IC Design Errors	D. C. Shaver S. P. Doran M. Rothschild J. H. C. Sedlacek	*Proc. SPIE* **1596**, 46 (1991)
Long-Wavelength Ge_xSi_{1-x}/Si Heterojunction Infrared Detectors and Focal Plane Arrays	B-Y. Tsaur C. K. Chen S. A. Marino	*Proc. SPIE* **1540**, 580 (1991)
Role of GaAs Bounding Layers in Improving OMVPE Growth and Performance of Strained-Layer InGaAs/AlGaAs Quantum-Well Diode Lasers	C. A. Wang H. K. Choi	*J. Electron. Mater.* **20**, 929 (1991)

ACCEPTED FOR PUBLICATION

Gain and Noise Figure in Analog Fiber-Optic Links	C. H. Cox III	*IEE Proc. J*
Real-Time Characterization of Acoustic Modes of Polyimide Thin Film Coatings Using Impulsive Stimulated Thermal Light Scattering	A. R. Duggal* J. A. Rogers* K. A. Nelson* M. Rothschild	*Appl. Phys. Lett.*
A Quantum-Flux-Parametron-Based Analog-to-Digital Converter with 18-GHz Sampling Rate and 5-GHz Bandwidth	Y. Harada* J. B. Green	*IEEE Trans. Appl. Supercond.*

*Author not at Lincoln Laboratory.

Sub-0.25-μm Resolution Using 193-nm Optical Lithography	M. A. Hartney M. W. Horn R. R. Kunz M. Rothschild D. C. Shaver	*Solid State Technol.*
Vapor Etching of GaAs and AlGaAs by CH_3I	C. W. Krueger C. A. Wang M. Flytzani-Stephanopoulos*	*Appl. Phys. Lett.*
High-Brightness Diode-Laser-Pumped Semiconductor Heterostructure Lasers	H. Q. Le W. D. Goodhue S. DiCecca	*Appl. Phys. Lett.*
Reactions of Hydrogenated Defects in Fused Silica Caused by Thermal Treatment and Deep UV Irradiation	D. H. Levy* K. K. Gleason* M. Rothschild J. H. C. Sedlacek R. Takke*	*Appl. Phys. Lett.*
New Materials for Diode-Pumped Solid State Lasers	C. A. Wang S. H. Groves	*IEEE J. Quantum Electron.*
Substrate Temperature Measurements Using Ultrasonically Bonded Platinel II Thermocouples	A. C. Westerheim A. C. Anderson M. J. Cima*	*Rev. Sci. Instrum.*
Frequency Tuning of Microchip Lasers Using Pump-Power Modulation	J. J. Zayhowski J. A. Keszenheimer	*IEEE J. Quantum Electron.*

*Author not at Lincoln Laboratory.

PRESENTATIONS†

CW Operation of GaSb-Based Diode Lasers at 2.2 μm (300 K) and 4.0 μm (80 K)	H. K. Choi S. J. Eglash	
Strained InGaAs/AlGaAs Quantum-Well Diode Lasers on Si with Longer Lifetimes	H. K. Choi C. A. Wang N. H. Karam*	
Effects on the Operation of an External-Cavity Laser of Phase Differences Between Multiple Inputs into the Cavity	C. J. Corcoran R. H. Rediker K. Rauschenbach	
Recent Advances in Excimer Laser Lithography	D. J. Ehrlich	
InGaAs-Diode-Laser-Pumped Yb:YAG Lasers	T. Y. Fan P. Lacovara H. K. Choi C. A. Wang R. L. Aggarwal	IEEE Lasers and Electro-Optics Society Annual Meeting, San Jose, California, 4-7 November 1991
Development of Mesospheric Sodium Laser Beacon for Atmospheric Adaptive Optics	T. H. Jeys	
Integrated-Optical Modulators for an Adaptive Nulling System	L. M. Johnson H. V. Roussell G. E. Betts W. K. Hutchinson A. Sonnenschein	
Recent Advances in Solid State Lasers for Radar Applications	A. Mooradian	

*Author not at Lincoln Laboratory.

†Titles of presentations are listed for information only. No copies are available for distribution.

Solid-State Microchip Laser Arrays	C. D. Nabors J. J. Zayhowski R. L. Aggarwal J. P. Donnelly V. Diadiuk A. Mooradian	IEEE Lasers and Electro-Optics Society Annual Meeting, San Jose, California, 4-7 November 1991
White-Light Integrated-Optical Mach-Zehnder Interferometer	R. H. Rediker L. M. Eriksen T. A. Lind L. M. Johnson	
InGaAs and AlInGaAs Strained Quantum-Well Diode Lasers	C. A. Wang H. K. Choi J. N. Walpole	
Observations of Optical Pumping of Mesospheric Sodium	T. H. Jeys R. M. Heinrichs	Optical Society of America Annual Meeting, San Jose, California, 4-7 November 1991
Optical Lithography at Feature Sizes of 0.25 μm and Below	D. C. Shaver	Meeting, Bay Area Chrome Users Society, Sunnyvale, California, 12 November 1991
Wafer-Scale Solid-State Mass-Memory System	T. M. Lyszczarz	Technical Seminar, CERAM, Colorado Springs, Colorado, 12 November 1991
MBE Growth of GaSb-Based Diode Lasers Emitting from 2 to 4 μm	S. J. Eglash	Lincoln Laboratory Technical Seminar Series, University of Illinois, Urbana, Illinois, 13 November 1991
CH_3I Vapor Etching of GaAs and AlGaAs	M. Flytzani-Stephanopoulos* C. W. Krueger C. A. Wang	Annual Meeting of the American Institute of Chemical Engineers, Los Angeles, California, 17-22 November 1991

*Author not at Lincoln Laboratory.

Device Applications and Characterization of GaAs Grown at Low Temperatures by Molecular Beam Epitaxy	F. W. Smith	Heterostructure Seminar Series, Massachusetts Institute of Technology, Cambridge, Massachusetts, 18 November 1991
Organometallic Vapor Phase Epitaxy of InGaAs and AlInGaAs Strained Quantum-Well Diode Lasers	C. A. Wang	Lincoln Laboratory Technical Seminar Series, University of Massachusetts, Amherst, Massachusetts, 18 November 1991
Device Applications and Characterization of GaAs Grown at Low Temperatures by Molecular Beam Epitaxy	F. W. Smith	IEEE Electron Devices Society, Boston Chapter Meeting, Waltham, Massachusetts, 21 November 1991
Plasma Chemistry in Microelectronic Processing: Reactive Ion Etching	M. A. Hartney	American Chemical Society Symposium on Chemistry and Electronics, Boston, Massachusetts, 23 November 1991
Plasma Chemistry in Microelectronic Processing: Chemical Vapor Deposition	M. W. Horn	
Recent Developments in Strained Quantum-Well Diode Lasers	H. K. Choi	Symposium, Korean Scientists and Engineers Association, Washington, D.C., 30 November-1 December 1991
CCD Neural Network Processors for Pattern Recognition	A. M. Chiang M. L. Chuang J. R. LaFranchise	IEEE Neural Information Processing Systems '91, Denver, Colorado, 2-5 December 1991
Low-Temperature-Grown GaAs and Related Materials	A. R. Calawa	1991 Fall Meeting of the Materials Research Society, Boston, Massachusetts, 2-6 December 1991
Overview and Recent Developments in Low-Temperature-Grown GaAs	A. R. Calawa	

In-Situ Substrate Temperature Measurement in High-T_c Superconducting Deposition	B. I. Choi* A. C. Anderson A. C. Westerheim M. I. Flik* Z. M. Zhang*	1991 Fall Meeting of the Materials Research Society, Boston, Massachusetts,2-6 December 1991
High-Temperature Optical Properties of $LaAlO_3$ and $SrTiO_3$	B. I. Choi* Z. M. Zhang* M. I. Flik* A. C. Anderson	
Selective-Area Growth of Metal Oxide Films Induced by Patterned Excimer Laser Surface Photolysis	R. R. Kunz D. J. Ehrlich J. Melngailis M. W. Horn	
Surface Impedance Overview: Measurement Methods, Relationship to Material Properties, and Theoretical Predictions	D. E. Oates	
Growth Techniques for Large-Area Mosaic Diamond Films	R. W. Pryor* M. W. Geis	
Microwave Circuits with High-Temperature Superconductors	R. W. Ralston	
The Device Applications of Low-Temperature-Grown GaAs	F. W. Smith	
Piezoelectric Thin Film Ultrasonic Micromotors	K. R. Udayakumar* J. Chen* K. G. Brooks* L. E. Cross* A. M. Flynn* S. F. Bart* L. S. Tavrow* R. A. Brooks* D. J. Ehrlich	

*Author not at Lincoln Laboratory.

Surface Defects in Sputter-Deposited Y-Ba-Cu-O Thin Films	A. C. Westerheim S. N. Basu* D. Bhatt* M. C. Finn L. S. Yu-Jahnes R. L. Slattery M. J. Cima* A. C. Anderson	1991 Fall Meeting of the Materials Research Society, Boston, Massachusetts,2-6 December 1991
A High Flux Atomic Oxygen Source for the Deposition of In Situ Superconducting High T_c Films	L. S. Yu-Jahnes W. T. Brogan A. C. Westerheim M. J. Cima* A. C. Anderson	
Infrared Refractive Indices of $LaAlO_3$, $LaGaO_3$, and $NdGaO_3$	Z. M. Zhang* B. I. Choi* M. I. Flik* A. C. Anderson	
Buried-Channel CCDs with High Charge Transfer Efficiency and Large Charge Capacity for Low-Temperature Readout of Long-Wavelength Infrared Detectors	A. L. Lattes B-Y. Tsaur	International Electron Devices Meeting, Washington, D.C., 8-10 December 1991
An Integrated Electronic Shutter for Back-Illuminated Charge-Coupled Devices	R. K. Reich R. W. Mountain W. H. McGonagle C. M. Huang J. C. Twichell B. B. Kosicki E. D. Savoye	
Surface Impedance of YBCO Thin Films	A. C. Anderson	Colloquium, Materials Science Department, Massachusetts Institute of Technology, Cambridge, Massachusetts, 9 December 1991

*Author not at Lincoln Laboratory.

Dry-Developed Organosilicon Resists for 193-nm Excimer Laser Lithography	R. R. Kunz M. W. Horn	Meeting, Semiconductor Association of New England, Andover, Massachusetts, 9 December 1991
Quantum Well Nonlinearities for Picosecond Multi-THz Frequency Shifting in Optical Communications	H. Q. Le	Lasers '91, San Diego, California, 9-13 December 1991
Gain and Noise Figure in Analog Fiber-Optic Links	C. H. Cox III	Second Annual DARPA/Rome Laboratory Symposium, Monterey, California, 10-12 December 1991
An Externally Modulated Fiber-Optic Link Test Bed for Addressing Application Issues and Options	C. H. Cox III L. A. Bernotas G. E. Betts A. I. Grayzel D. R. O'Brien J. J. Scozzafava A. C. Yee	
Microchip Lasers	J. J. Zayhowski	Optics and Quantum Electronics Seminar, Massachusetts Institute of Technology, Cambridge, Massachusetts, 11 December 1991
Resonant-Tunneling-Diode Circuits	T. C. L. G. Sollner E. R. Brown R. A. Calawa C. L. Chen C. G. Fonstad* W. D. Goodhue R. H. Mathews J. P. Sage F. W. Smith	International Workshop on Quantum-Effect Physics, Electronics, and Applications, Luxor, Egypt, 6-10 January 1992
Suppression of Acoustic Effects in Lithium Niobate Integrated Optical Modulators	G. E. Betts	IEEE Ultrasonics, Ferroelectrics, and Frequency Control Society, Boston Chapter Meeting, Lexington, Massachusetts, 22 January 1992

*Author not at Lincoln Laboratory.

Measurement of RHEED Oscillations During MBE Growth of GaAs on a Rotating Substrate	G. W. Turner A. J. Isles*	19th Conference on Physics and Chemistry of Semiconductor Interfaces, Death Valley, California, 28-30 January 1992

*Author not at Lincoln Laboratory.

ORGANIZATION

SOLID STATE DIVISION

A. L. McWhorter, *Head*
I. Melngailis, *Associate Head*
E. Stern, *Associate Head*
D. C. Shaver, *Assistant Head*
J. F. Goodwin, *Assistant*

D. J. Ehrlich, *Senior Staff*
N. L. DeMeo, Jr., *Associate Staff*
J. W. Caunt, *Assistant Staff*
K. J. Challberg, *Administrative Staff*

SUBMICROMETER TECHNOLOGY

M. Rothschild, *Leader*
T. M. Lyszczarz, *Assistant Leader*

Astolfi, D. K.
Craig, D. M.
Dennis, C. L.
DiNatale, W. F.
Doran, S. P.
Efremow, N. N., Jr.
Forte, A. R.
Gajar, S. A.*
Geis, M. W.
Goodman, R. B.
Hartney, M. A.
Horn, M. W.
Kunz, R. R.
Maki, P. A.
Melngailis, J.†
Sedlacek, J. H. C.
Uttaro, R. S.

QUANTUM ELECTRONICS

A. Mooradian, *Leader*
P. L. Kelley, *Associate Leader*
A. Sanchez-Rubio, *Assistant Leader*

Aggarwal, R. L.
Barch, W. E.
Cook, C. C.
Daneu, V.
DeFeo, W. E.
DiCecca, S.
Dill, C. D., III
Fan, T. Y.
Hancock, R. C.
Henion, S. R.
Hotaling, T. C.
Hsu, L.*
Jeys, T. H.
Korn, J. A.
Lacovara, P.
Le, H. Q.
Nabors, C. D.
Ochoa, J. R.
Schulz, P. A.
Sullivan, D. J.
Wall, K. F.
Zayhowski, J. J.

ELECTRONIC MATERIALS

A. J. Strauss, *Leader*
B-Y. Tsaur, *Associate Leader*

Anderson, C. H., Jr.
Button, M. J.
Chen, C. K.
Choi, H. K.
Clark, H. R., Jr.
Connors, M. K.
Eglash, S. J.
Fahey, R. E.
Finn, M. C.
Iseler, G. W.
Kolesar, D. F.
Krohn, L., Jr.
Marino, S. A.
Mastromattei, E. L.
McGilvary, W. L.
Nitishin, P. M.
Pantano, J. V.
Turner, G. W.
Wang, C. A.

HIGH SPEED ELECTRONICS

R. A. Murphy, *Leader*
M. A. Hollis, *Assistant Leader*
R. W. Chick, *Senior Staff*

Actis, R.
Bergeron, N. J.
Bozler, C. O.
Brown, E. R.
Calawa, A. R.
Chen, C. L.
Clifton, B. J.‡
Goodhue, W. D.
Gray, R. V.
Lincoln, G. A., Jr.
Mahoney, L. J.
Manfra, M. J.
Mathews, R.H.
Mattia, J. P.*
McIntosh, K. A.
McMorran, R. A.
McNamara, M. J.
Nichols, K. B.
Parker, C. D.
Rabe, S.
Rathman, D. D.
Smith, F. W., III
Vera, A.

---

* Research Assistant
† Part Time
‡ Leave of Absence

ELECTROOPTICAL DEVICES

R. C. Williamson, *Leader*
D. L. Spears, *Assistant Leader*
R. H. Rediker, *Senior Staff*

Aull, B. F.
Bailey, R. J.
Betts, G. E.
Corcoran, C. J.*
Cox, C. H., III
Donnelly, J. P.
Ferrante, G. A.
Groves, S. H.
Harman, T. C.
Hovey, D. L.
Johnson, L. M.
Liau, Z. L.
Lind, T. A.
Missaggia, L. J.
Mull, D. E.
O'Donnell, F. J.
Palmacci, S. T.
Palmateer, S. C.
Pheiffer, B. K.*
Reeder, R. E.
Roussell, H. V.
Shiple, S. D.*
Tsang, D. Z.
Walpole, J. N.
Woodhouse, J. D.
Yee, A. C.

ANALOG DEVICE TECHNOLOGY

R. W. Ralston, *Leader*
R. S. Withers, *Associate Leader*‡
T. C. L. G. Sollner, *Assistant Leader*
A. C. Anderson, *Senior Staff*
R. M. Lerner, *Senior Staff*†

Arsenault, D. R.
Bhushan, M.‡
Boisvert, R. R.
Brogan, W. T.
Denneno, A. P.
Denneno, J. M.
Fitch, G. L.
Green, J. B.
Holtham, J. H.
Lattes, A. L.
Lyons, W. G.
Macedo, E. M., Jr.
Minnick, R. G.
Oates, D. E.
Sage, J. P.
Seaver, M. M.
Slattery, R. L.
Westerheim, A. C.*
Whitley, D. B.
Yu-Jahnes, L. S.*

MICROELECTRONICS

E. D. Savoye, *Leader*
B. B. Kosicki, *Assistant Leader*
B. E. Burke, *Senior Staff*
A. M. Chiang, *Senior Staff*

Chuang, M. L.*
Collins, I. K.
Cooper, M. J.
Daniels, P. J.
Doherty, C. L., Jr.
Dolat, V. S.
Donahue, T. C.
Durant, G. L.
Felton, B. J.
Gregory, J. A.
Huang, C. M.
Hurley, E. T.
Johnson, B. W.
Johnson, K. F.
LaFranchise, J. R.
Loomis, A. H.
McGonagle, W. H.
Mountain, R. W.
Percival, K. A.
Pichler, H. H.
Reich, R. K.
Reinold, J. H., Jr.
Young, D. J.

---

* Research Assistant
† Part Time
‡ Leave of Absence

1. ELECTROOPTICAL DEVICES

1.1 TOLERANCE FOR RESIDUAL RIPPLES IN MASS-TRANSPORTED MICROLENSES

Microlenses fabricated by mass-transport smoothing of multilevel mesa structures in semiconductor substrates have high indices and accurate profiles and are potentially well suited for large-numerical-aperture microoptical applications [1]. Because of the very strong spatial dependence of the mass-transport process [2], longer times are needed to totally smooth out wide steps in the fabrication of large-aperture (a few hundred micrometers) microlenses. Knowledge of acceptable incomplete smoothing can therefore result in practical time-saving measures. In this work, we develop an analytical model for the effect of residual ripples and obtain simple expressions for power losses in the collimated beam and for the scattered radiation.

As illustrated in Figure 1-1(a), the etched multistep structure usually has a constant step width Δ. The step height, on the other hand, is directly proportional to the distance from the center, because the designed lens profile is usually very close to parabolic. In mass-transport smoothing the corners first become rounded, and the multistep surface profile becomes sinusoidal. The amplitude then undergoes an exponential decay, and a completely smooth lens surface is finally formed [1],[2]. When an incompletely smoothed lens is used in beam collimation, the ripple results in additional optical path length variations and hence a corresponding ripple in an otherwise collimated, flat wavefront in the near field, as illustrated in Figure 1-1(b). Here, we first consider the simple case of a cylindrical lens uniformly illuminated by the incident beam. Gaussian-beam illumination will be treated later.

By superposition of waves originating at points across the aperture, as illustrated in Figure 1-1(b), the far-field amplitude is given by

$$E(\theta)=\frac{E_0}{L}\int_{-D/2}^{D/2}\exp\left\{\frac{2\pi i}{\lambda}\left[x\sin\theta+(n-1)\frac{x\delta}{D}\sin\frac{2\pi x}{\Delta}\right]\right\}dx\ , \tag{1.1}$$

where E_0 is the central maximum without the residual ripples (i.e., when $\delta=0$), D is the microlens aperture, λ is the wavelength of light in vacuum, n is the refractive index of the lens material, and δ is the maximum full amplitude of the residual ripple. Since only ripples with amplitude δ much smaller than the wavelength λ are considered, we have

$$\exp\left[\frac{2\pi i}{\lambda}(n-1)\frac{x\delta}{D}\sin\frac{2\pi x}{\Delta}\right]\approx 1-\frac{1}{4}\left[\frac{2\pi(n-1)x\delta}{\lambda D}\right]^2+\frac{1}{4}\left[\frac{2\pi(n-1)x\delta}{\lambda D}\right]^2\cos\frac{4\pi x}{\Delta}$$

$$+i\left[\frac{2\pi(n-1)x\delta}{\lambda D}\right]\sin\frac{2\pi x}{\Delta}\ . \tag{1.2}$$

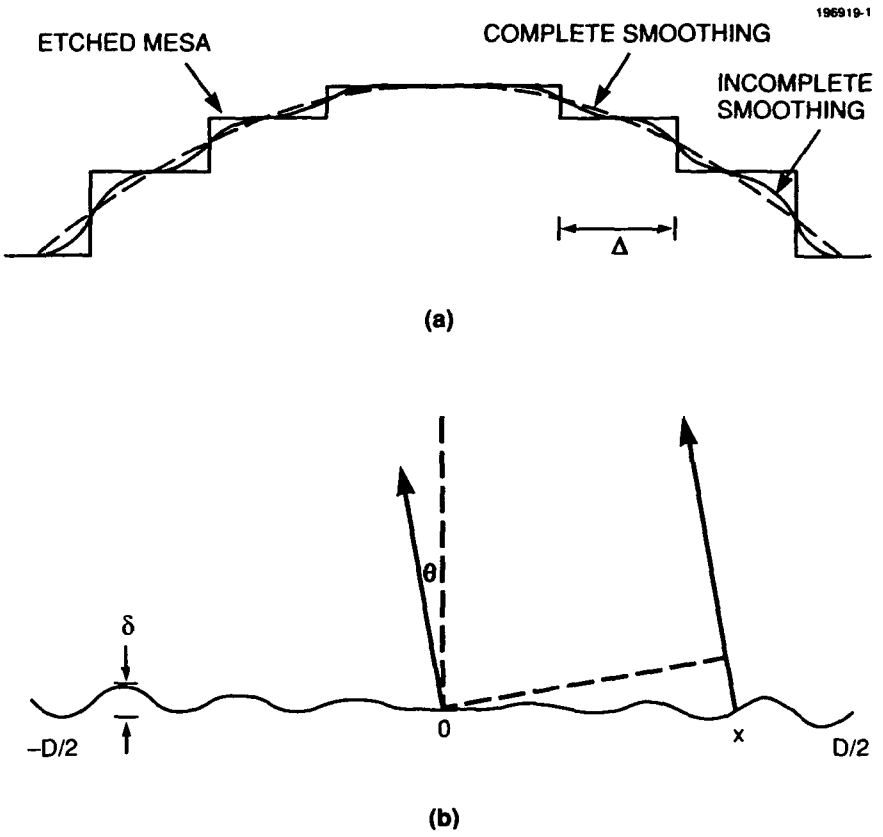

Figure 1-1. (a) Residual ripple in a microlens due to incomplete mass-transport smoothing. (b) Effect of the residual ripple on beam collimation. In actual microlens fabrication, the step width Δ is typically 10 μm and the step heights range from 0.2 to 3 μm.

It can readily be shown that the third term on the right-hand side gives rise to very low intensity scattered light at large angles and can therefore be neglected. By substituting Equation (1.2) into (1.1), the integral is readily evaluated term by term to yield

$$E(\theta) \approx E_0 \frac{\sin\xi}{\xi} - E_0\left[\frac{\pi(n-1)\delta}{2\lambda}\right]^2 \frac{2\xi\cos\xi + (\xi^2-2)\sin\xi}{\xi^3}$$

$$+iE_0 \frac{\pi(n-1)\delta}{2\lambda}\left(\frac{\sin\xi' - \xi'\cos\xi'}{\xi'^2} - \frac{\sin\xi'' - \xi''\cos\xi''}{\xi''^2}\right), \qquad (1.3)$$

where $\xi \equiv \pi\theta D/\lambda$, $\xi' \equiv \xi + 2N\pi$, and $\xi'' \equiv \xi - 2N\pi$. Here, $N \equiv (1/2)D/\Delta$, the number of steps in the original etched structure. The first term on the right-hand side of Equation (1.3) is the well-known diffraction pattern of an aperture of width D and is the collimated beam from an ideal microlens without the residual ripple. The second term, which is due to the ripple, brings the amplitude down slightly [see Equation (1.4) below] but otherwise effects little change in that pattern. The third term represents a pair of scattered beam

patterns centered at $\xi = \pm 2N\pi$, where the maximum amplitude is $[0.22\pi(n-1)\delta/\lambda]E_0$. Note that the factor i represents a temporal 90° phase shift with respect to the central beam. An entire far field calculated for $\delta = \lambda/20$, $n = 3.2$, and $N = 5$ is illustrated in Figure 1-2(a).

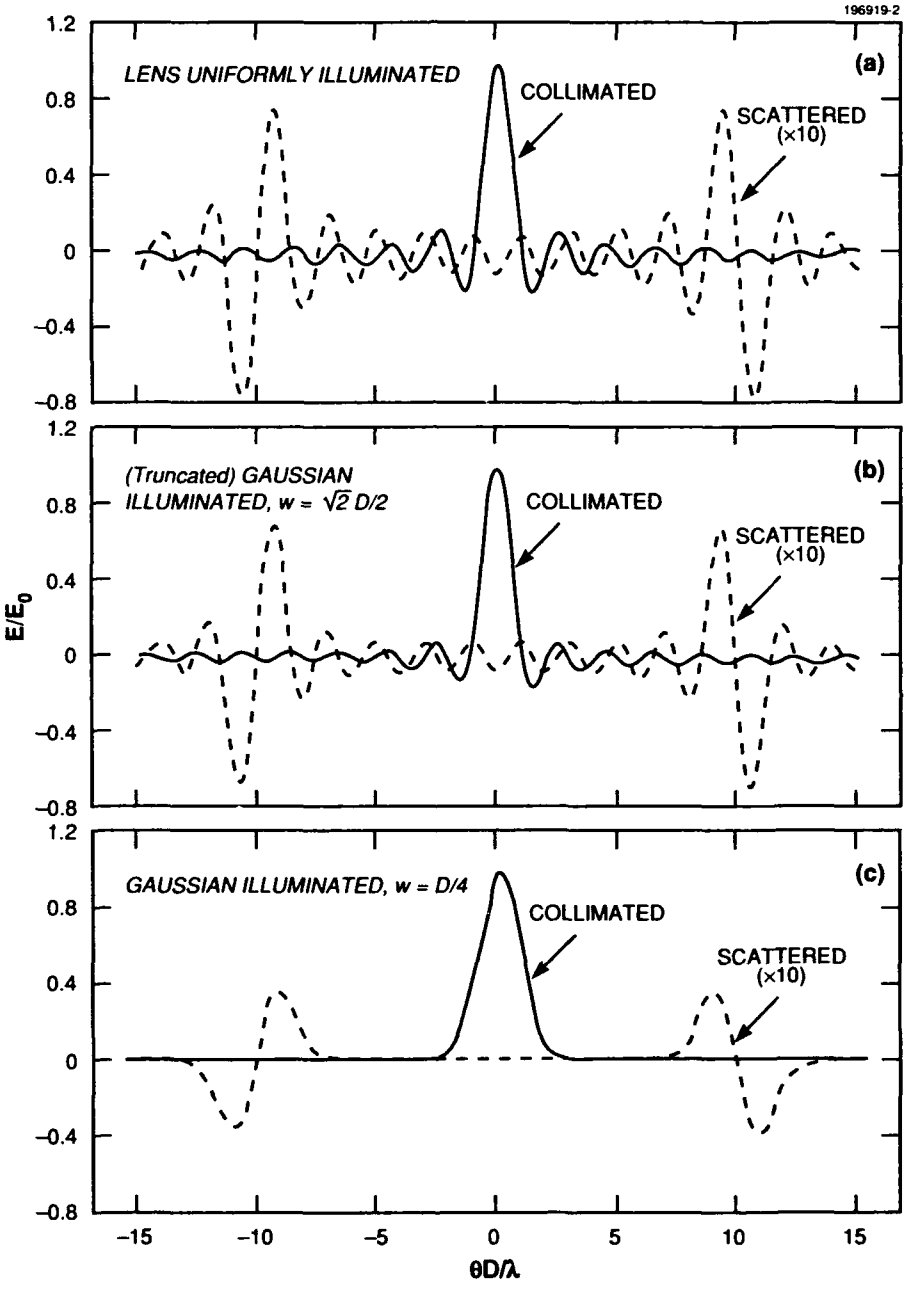

Figure 1-2. (a) Calculated far-field amplitude of a uniformly illuminated cylindrical microlens with a residual ripple of $\delta = \lambda/20$, $n = 3.2$, and $\Delta = D/10$. The scattered light, as given by the third term on the right-hand side of Equation (1.3), has a temporal 90° phase shift with respect to the collimated beam. (b) Same far field as in (a) but with a truncated Gaussian illumination on the microlens. (c) Far field of the microlens under Gaussian illumination.

The central maximum is obtained by substituting $\theta = 0$ in Equation (1.3):

$$E(0) \approx E_0\left\{1-\frac{1}{3}\left[\frac{\pi(n-1)\delta}{2\lambda}\right]^2\right\}-iE_0\left[\frac{(n-1)\delta}{2N\lambda}\right]. \tag{1.4}$$

Note that the real part, which is the dominant term, is determined by the mean-square deformation of the wavefront [3].

When the microlens is used to collimate a Gaussian beam of width w, the far-field amplitude is given by

$$E(\theta) = E_0\frac{\int_{-D/2}^{D/2}\exp\left(-\frac{x^2}{w^2}\right)\exp\left\{\frac{2\pi i}{\lambda}\left[x\sin\theta+(n-1)\frac{x\delta}{D}\sin\frac{2\pi x}{\Delta}\right]\right\}dx}{\int_{-D/2}^{D/2}\exp\left(-\frac{x^2}{w^2}\right)dx}. \tag{1.5}$$

The integrals can be evaluated analytically for either $w > D/2$ or $w << D/2$.

When $w > D/2$, we have

$$\exp\left(-\frac{x^2}{w^2}\right)\approx 1-\frac{x^2}{w^2}. \tag{1.6}$$

By substituting Equations (1.2) and (1.6) into (1.5), the integrals can be evaluated term by term to yield

$$\begin{aligned}E(\theta) \approx\ & E_0\left(1-\frac{D^2}{12w^2}\right)^{-1}\frac{\sin\xi}{\xi}-E_0\left(1-\frac{D^2}{12w^2}\right)^{-1}\left\{\left[\frac{\pi(n-1)\delta}{2\lambda}\right]^2+\frac{D^2}{4w^2}\right\}\\ &\frac{2\xi\cos\xi+(\xi^2-2)\sin\xi}{\xi^3}+iE_0\left(1-\frac{D^2}{12w^2}\right)^{-1}\left[\frac{\pi(n-1)\delta}{2\lambda}\right]\\ &\left[\frac{\sin\xi'-\xi'\cos\xi'}{\xi'^2}-\left(\frac{D^2}{4w^2}\right)\frac{(3\xi'^2-6)\sin\xi'-(\xi'^3-6\xi')\cos\xi'}{\xi'^4}\right.\\ &\left.-\frac{\sin\xi''-\xi''\cos\xi''}{\xi''^2}+\left(\frac{D^2}{4w^2}\right)\frac{(3\xi''^2-6)\sin\xi''-(\xi''^3-6\xi'')\cos\xi''}{\xi''^4}\right]\end{aligned} \tag{1.7}$$

and

$$E(0) \approx E_0\left\{1-\frac{1}{3}\left[\frac{\pi(n-1)\delta}{2\lambda}\right]^2\left(1-\frac{D^2}{15w^2}\right)\right\} . \tag{1.8}$$

The far-field pattern calculated for $\delta = \lambda/20$, $n = 3.2$, $N = 5$, and $w = \sqrt{2}\ D/2$ is shown in Figure 1-2(b). Note the close similarity to Figure 1-2(a), except for a somewhat wider central lobe and lower fringes.

When $w << D/2$, the integration limits in Equation (1.5) can be taken as $\pm\infty$, and the integrals can be evaluated, with the aid of tables of definite integrals [4], to yield

$$\begin{aligned} E(0) \approx E_0 e^{-\zeta^2} &- \frac{E_0}{2}\left[\frac{\pi(n-1)\delta}{2\lambda}\right]^2\left(\frac{2w}{D}\right)\left(1-2\zeta^2\right)e^{-\zeta^2} \\ &-iE_0\left[\frac{\pi(n-1)\delta}{2\lambda}\right]\left(\frac{2w}{D}\right)\left(\zeta' e^{-\zeta'^2} - \zeta'' e^{-\zeta''^2}\right) , \end{aligned} \tag{1.9}$$

where $\zeta \equiv \pi w\theta/\lambda$, $\zeta' \equiv \zeta + 2N\pi w/D$, and $\zeta'' \equiv \zeta - 2N\pi w/D$. The central maximum is then given by

$$E(0) \approx E_0\left\{1-\frac{1}{2}\left[\frac{\pi(n-1)\delta}{2\lambda}\right]^2\left(\frac{2w}{D}\right)^2\right\} . \tag{1.10}$$

The field distribution calculated for $\delta = \lambda/20$, $n = 3.2$, $N = 5$, and $w = D/4$ is shown in Figure 1-2(c). Note the smaller scattering compared to those in Figures 1-2(a) and 1-2(b).

The effect of the residual ripple is smaller for Gaussian-beam illumination because of the graded ripple amplitude. The effect can be kept small for either case by making the overall amplitude δ sufficiently small. For instance, with $\delta = \lambda/20$ (or 50 nm for $\lambda = 1\ \mu$m), the fractional power loss $1-\left[E(0)/E_0\right]^2$, as calculated from Equation (1.4), is only 2%.

In conclusion, a simple technique has been developed to quantitatively assess acceptable incomplete smoothing in mass-transported microlenses. This can result in practical time-saving measures in the fabrication of large-aperture microlenses.

Z. L. Liau

1.2 INTEGRATED-OPTICAL MODULATOR CANCELLATION MEASUREMENTS

An adaptive nulling system based on optical technology is being developed for microwave/millimeter-wave multielement antenna systems [5]. This nulling technique involves intensity modulating separate optical carrier waves with each of the antenna RF signals. Once the RF signals are on an optical carrier, nulling operations such as complex weighting, time delay, and summing are implemented optically, taking advantage of the small fractional bandwidth of the modulated optical signal to more easily achieve channel tracking. Previously [6], we demonstrated that integrated-optical interferometric intensity modulators provide the

channel tracking required in both amplitude and phase to achieve null depths > 40 dB over the frequency band 5 to 7 GHz. In this report, the results of a signal cancellation experiment utilizing these modulators are described.

The cancellation measurement arrangement is illustrated in Figure 1-3 and consists of two optical channels, each comprising a matched traveling-wave interferometric modulator as well as a low-speed modulator to provide relative amplitude weighting. To maximize cancellation, a single diode-pumped Nd:YAG laser source provides the optical power, which is split between the two channels. Similarly, the modulator RF drive signals are provided by a single source. The optical signals from the two channels are combined noncoherently in a multimode fiber coupler and measured on a single photodetector. By biasing the front-end modulators on opposite slopes, a 180° phase shift is obtained between the two channels so that cancellation can be realized. Dispersion effects are minimized by carefully matching the path lengths of the two channels between the RF splitter and the optical combiner.

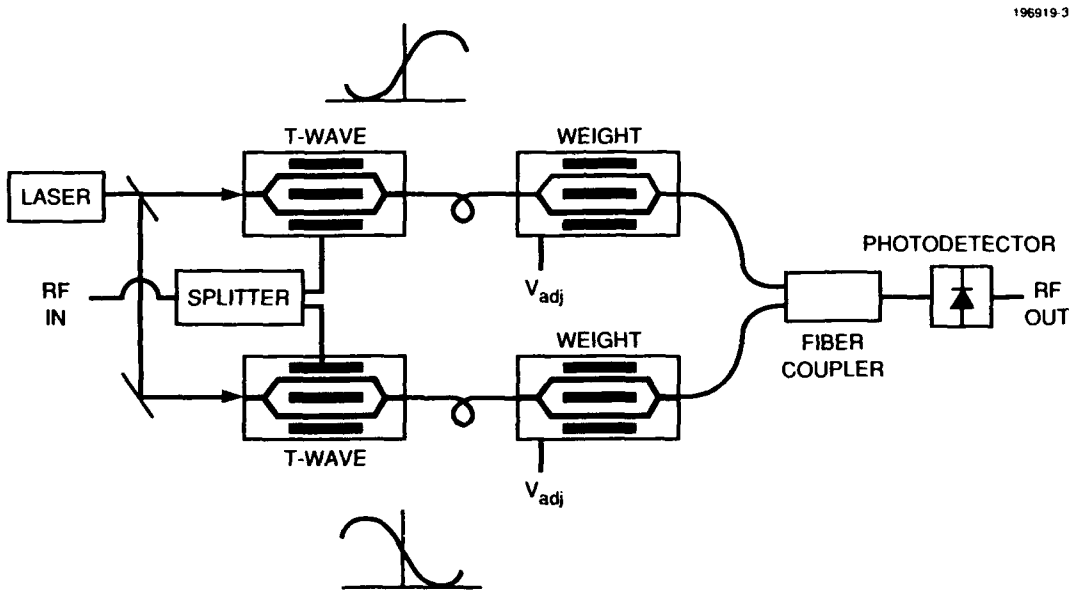

Figure 1-3. Illustration of the system for optical modulator cancellation measurement.

Results are shown in Figure 1-4 for signal cancellation measurements over the frequency band 5 to 7 GHz. The upper trace shows the detector output measured on the network analyzer for the case where both channels are in phase (both modulators biased with the same slope), and the lower trace shows the maximum cancellation obtained with the 180° bias condition. Cancellation varies across the frequency band, but an average of ~ 36 dB is obtained. This is an encouraging result for nulling systems applications. As expected, measured channel cancellation was a strong function of both the relative amplitude weighting and the path length difference between the two channels.

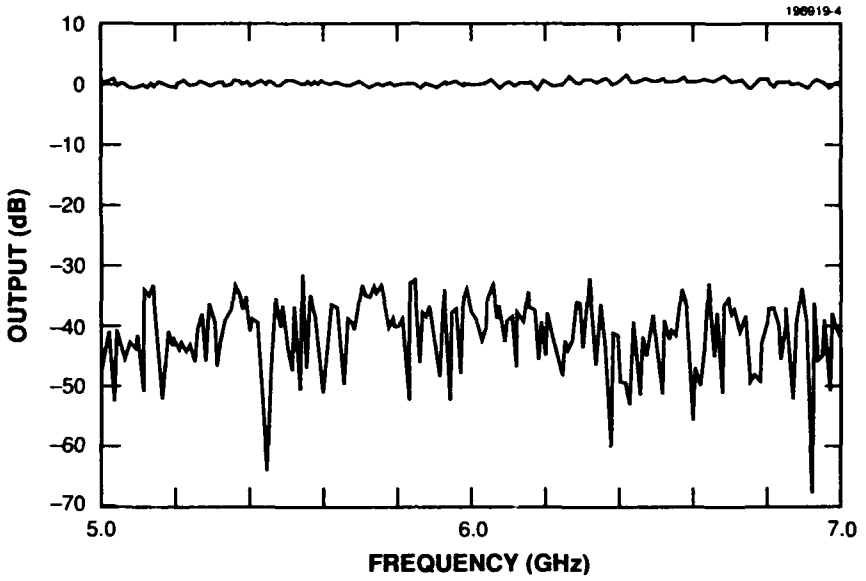

Figure 1-4. Network analyzer cancellation measurements. The upper trace shows the detector output when both channels are in phase, and the lower trace shows the maximum cancellation obtained with the 180° bias condition.

Based on modulator measurements alone, cancellation across the band is predicted to be ~ 50 dB. Other system factors, including optical scattering, multiple reflections, and detector speckle effects, are being investigated to explain the discrepancy.

L. M. Johnson W. K. Hutchinson
H. V. Roussell A. Sonnenschein

1.3 InGaAs/GaInAsP/GaInP DIODE LASERS

Aluminum-free GaAs-based strained-layer single-quantum-well (SSQW) separate-confinement heterostructure (SCH) lasers grown by organometallic vapor phase epitaxy (OMVPE) have been previously reported [7]. These devices, with emission in the 980-nm range of interest for pumping Er-doped fiber amplifiers, utilize $In_{0.18}Ga_{0.82}As$ as the strained-layer quantum-well material, GaAs for the separate-confinement region, and $Ga_{0.51}In_{0.49}P$ for the cladding. The threshold current densities $J_{th} < 100$ A/cm^2 were very low, but the measured differential quantum efficiencies $\eta_d < 35\%$/facet were below the 40 to 45%/facet values for the best AlGaAs lasers.

The choice of GaAs as the separate-confinement layer material simplifies the epitaxial growth of the first structures. For an $Al_xGa_{1-x}As$ SCH structure, the confinement layers are typically an alloy with $x \approx 0.2$. A comparable aluminum-free SSQW SCH laser structure can also be made using a GaInAsP quaternary alloy as the confinement-layer material. A first report of such devices is given here, and broad-area characterization results are presented. Very high η_d in excess of 40%/facet is obtained.

The device structure investigated is shown in Figure 1-5. The $Ga_xIn_{1-x}As_yP_{1-y}$ alloy with $x \approx 0.7$ and $y \approx 0.3$ has an energy gap of 1.65 eV, which is about the same as that of $Al_{0.2}Ga_{0.8}As$. For these first structures with the GaInAsP alloy instead of GaAs, the confinement-layer thickness was increased to 0.2 μm from

0.1 μm to compensate for the smaller refractive-index step at the confinement-cladding junction. The structure was grown in a chimney-type OMVPE reactor incorporating susceptor rotation and operating at atmospheric pressure [8]. The growth temperature was 650°C for all layers except the p-type GaAs contact layer. To increase the zinc-acceptor incorporation, the contact layer was grown at 600°C, which gives $p^+ \approx 5 \times 10^{19}$ cm^{-3} and a low specific contact resistance of 5×10^{-5} Ω cm^2. Details of the OMVPE growth of the SCH SSQW structures with GaInAsP alloy confinement layers have been reported recently [9].

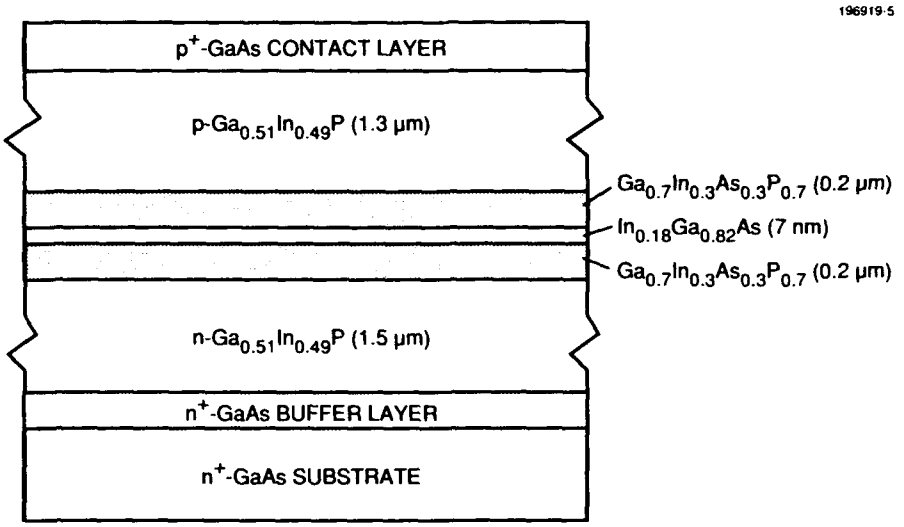

Figure 1-5. Aluminum-free GaAs-based SSQW SCH structure with 1.65-eV bandgap $Ga_{0.7}In_{0.3}As_{0.3}P_{0.7}$ alloy used as the confinement-layer material.

The measured single-ended output power vs input current for a broad-area device is shown in Figure 1-6. A 225-μm-wide stripe was defined by etched isolation grooves, and the device cleaved to a 660-μm cavity length. For this device $J_{th} = 230$ A/cm^2, which is about twice that reported in [7] for devices of the same length. This increase is attributed to the reduced confinement factor that results from the larger confinement-layer width.

The notable feature of Figure 1-6 is the large increase in η_d over the values for the GaAs-confinement-layer structures. The deeper quantum well that results from using GaInAsP, rather than GaAs, as the confinement layer is thought to account for the improved efficiency. An alternative explanation is that the free-carrier absorption is reduced in the structure with the wider, undoped confinement layers. However, increasing this width in the GaAs-confinement devices has produced no increase in η_d. Experiments are now under way to establish the effect of the confinement width and to optimize the structure with the quaternary confinement layers.

S. H. Groves
J. N. Walpole
A. Napoleone
L. J. Missaggia
P. S. Day

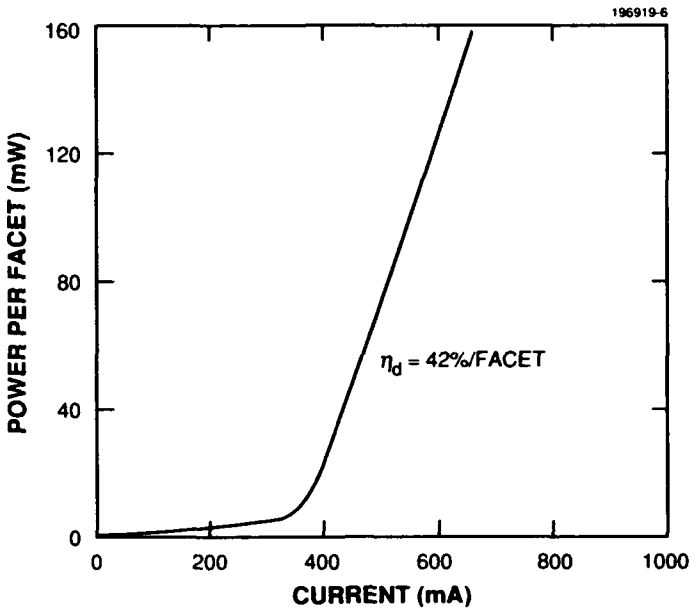

Figure 1-6. Single-ended output power vs input current for a broad-area device having the structure of Figure 1-5, 660-μm length, and 225-μm width.

REFERENCES

1. Z. L. Liau, V. Diadiuk, J. N. Walpole, and D. E. Mull, *Appl. Phys. Lett.* **55**, 97 (1989).
2. Z. L. Liau and H. J. Zeiger, *J. Appl. Phys.* **67**, 2434 (1990).
3. M. Born and E. Wolf, *Principles of Optics*, 6th ed. (Pergamon, Oxford, 1980), p. 463.
4. H. B. Dwight, *Tables of Integrals and Other Mathematical Data*, 4th ed. (MacMillan, New York, 1961), Chap. 12.
5. A. Sonnenschein and W. K. Hutchinson, MIT Lincoln Laboratory Technical Report 887, August 1990.
6. Solid State Research Report, Lincoln Laboratory, MIT, 1991:2, p. 1.
7. Z. L. Liau, S. C. Palmateer, S. H. Groves, J. N. Walpole, and L. J. Missaggia, *Appl. Phys. Lett.* **60**, 6 (1992).
8. S. C. Palmateer, S. H. Groves, J. W. Caunt, and D. L. Hovey, *J. Electron. Mater.* **18**, 645 (1989).
9. Solid State Research Report, Lincoln Laboratory, MIT, 1991:4, p. 6.

2. QUANTUM ELECTRONICS

2.1 HIGH-POWER CW OPERATION OF MICROCHIP LASERS

Heat removal from laser rods is typically done by cooling the cylindrical surface of the rod. For the case of uniform pumping, where little heat or no heat is removed from the rod faces, the resulting temperature and stress distributions in the rod have only a radial dependence [1]. For end-pumped laser geometries, where the pump source for the laser is itself a laser, the distribution of heat within the laser rod is no longer uniform but often has a Gaussian distribution. If the heat deposition is uniform along the length of the rod (which is a good approximation for disk geometries), analytic solutions for the temperature and stress distributions can be obtained [2].

When Nd:YAG, one of the most common laser media, is used in a cylindrical geometry the normally isotropic crystalline host exhibits a radial birefringence resulting from the thermally induced stresses. This can have important consequences for applications in which the polarization of the laser beam is important (e.g., for Q switching and nonlinear frequency conversion). The birefringence can lead to an additional cavity loss if a polarizer is present in the laser cavity. Here, we derive an expression for the birefringence that results from Gaussian heat deposition in a Nd:YAG disk. We also calculate the round-trip loss associated with having a polarizer within the laser cavity, for the case of uniform illumination of the gain element approximating a multimode signal beam.

The problem of stress-induced birefringence in Nd:YAG rods for the case of uniform pumping has been previously considered by Koechner and Rice [3], Foster and Osterink [4], and Karr [5]. For a cylindrically symmetric pumping profile, the index of refraction for the radial and azimuthal directions can be expressed as [3]

$$n_r(r) = n_0 - \frac{n_0^3}{12}\left\{p_{11}\left[3\varepsilon_r(r) + \varepsilon_\phi(r) + 2\varepsilon_z(r)\right] + p_{12}\left[3\varepsilon_r(r) + 5\varepsilon_\phi(r) + 4\varepsilon_z(r)\right] + p_{44}\left[6\varepsilon_r(r) - 2\varepsilon_\phi(r) - 4\varepsilon_z(r)\right]\right\} \tag{2.1}$$

and

$$n_\phi(r) = n_0 - \frac{n_0^3}{12}\left\{p_{11}\left[\varepsilon_r(r) + 3\varepsilon_\phi(r) + 2\varepsilon_z(r)\right] + p_{12}\left[5\varepsilon_r(r) + 3\varepsilon_\phi(r) + 4\varepsilon_z(r)\right] - p_{44}\left[2\varepsilon_r(r) - 6\varepsilon_\phi(r) + 4\varepsilon_z(r)\right]\right\}, \tag{2.2}$$

where $n_r(r)$ and $n_\phi(r)$ are the radially dependent radial and azimuthal indices of refraction, respectively; n_0 is the index of refraction in the absence of perturbation; p_{11}, p_{12}, and p_{44} are the photoelastic coefficients for YAG; and $\varepsilon_r(r)$, $\varepsilon_\phi(r)$, and $\varepsilon_z(r)$ are the radially dependent elastic strains in the radial, azimuthal, and axial directions, respectively. For an isotropic or a cubic material, such as YAG, the elastic strains can be related to the stresses by

$$\varepsilon_r(r) = \frac{1}{E}\left\{\sigma_r(r) - \nu\left[\sigma_\phi(r) + \sigma_z(r)\right]\right\} , \tag{2.3}$$

$$\varepsilon_\phi(r) = \frac{1}{E}\left\{\sigma_\phi(r) - \nu\left[\sigma_r(r) + \sigma_z(r)\right]\right\} , \tag{2.4}$$

and

$$\varepsilon_z(r) = \frac{1}{E}\left\{\sigma_z(r) - \nu\left[\sigma_r(r) + \sigma_\phi(r)\right]\right\} , \tag{2.5}$$

where E is Young's modulus; $\sigma_r(r)$, $\sigma_\phi(r)$, and $\sigma_z(r)$ are the radially dependent radial, azimuthal, and axial stresses, respectively; and ν is Poisson's ratio. For a disk geometry with a radially dependent temperature distribution, $\sigma_z = 0$. Inserting Equations (2.3), (2.4), and (2.5) into Equations (2.1) and (2.2) yields

$$n_r(r) = n_0 - \frac{n_0^3}{12}\left[C_1\,\sigma_r(r) + C_2\,\sigma_\phi(r)\right] \tag{2.6}$$

and

$$n_\phi(r) = n_0 - \frac{n_0^3}{12}\left[C_2\,\sigma_r(r) + C_1\,\sigma_\phi(r)\right] , \tag{2.7}$$

where

$$C_1 \equiv p_{11}(1-\nu) + p_{12}(1-3\nu) + 2p_{44}(1+\nu) \tag{2.8}$$

and

$$C_2 \equiv p_{11}(1-5\nu) + p_{12}(5-7\nu) - 2p_{44}(1+\nu) . \tag{2.9}$$

The birefringence $B(r) \equiv n_r(r) - n_\phi(r)$ is simply

$$B(r) = \frac{n_0^3}{12}(C_2 - C_1)\left[\sigma_r(r) - \sigma_\phi(r)\right] . \tag{2.10}$$

Substitution of the previously derived expressions for the radial and azimuthal stresses [2] into Equation (2.10) gives for a Gaussian pumping distribution

$$B(r) = \frac{2\,n_0^3\,\alpha\,C_B\,P_h}{\pi\,K\,L}\left[\frac{\gamma(r) - 1 + e^{-\gamma(r)}}{\gamma(r)\left(1 - e^{-\xi}\right)}\right] , \tag{2.11}$$

where α is the coefficient of linear expansion, P_h is the total power dissipated as heat within the disk, K is the thermal conductivity, and L is the length of the disk. Also,

$$C_B \equiv \frac{(\nu+1)(p_{11}-p_{12}+4p_{44})}{48} , \tag{2.12}$$

$$\gamma(r) \equiv 2\left(\frac{r}{\omega_p}\right)^2 , \tag{2.13}$$

and

$$\xi \equiv 2\left(\frac{R}{\omega_p}\right)^2 , \tag{2.14}$$

where ω_p is the radius of the Gaussian pumping distribution and R is the radius of the disk. An example of the birefringence as a function of radius for a Nd:YAG disk with $R = 1$ cm, $L = 0.1$ cm, $\omega_p = 0.1$ cm, and $P_h = 10$ W is shown in Figure 2-1.

If a linear polarizer is inserted into a laser cavity containing an end-pumped Nd:YAG disk, the fractional intensity I_r of the 1.06-μm laser radiation rejected by the polarizer after the radiation makes a round-trip of the cavity, assuming uniform illumination of the disk by the laser, is [5]

$$I_r = \frac{1}{R^2}\int_0^R \sin^2[\delta(r)]\, r\, dr , \tag{2.15}$$

since the round-trip difference in retardation, $\delta(r) = 2\pi B(r) L/\lambda$, where λ is the laser wavelength, is independent of the azimuthal angle ϕ.

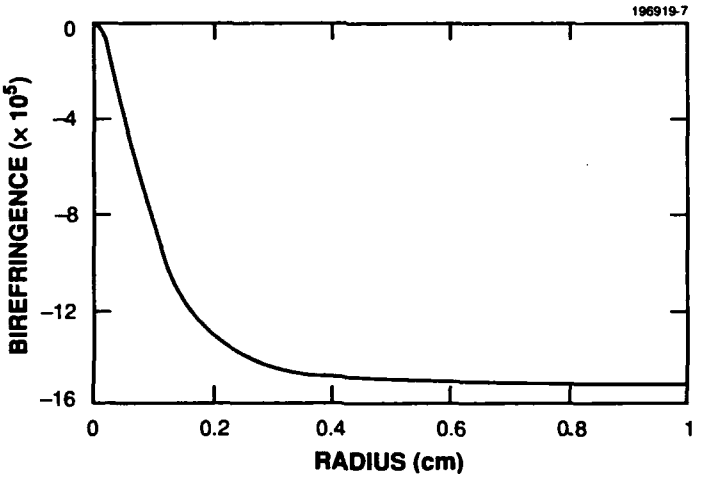

Figure 2-1. Example of stress-induced birefringence for a Nd:YAG disk heated with a Gaussian beam. In this example, $R = 1$ cm, $L = 0.1$ cm, $\omega_p = 0.1$ cm, and $P_h = 10$ W.

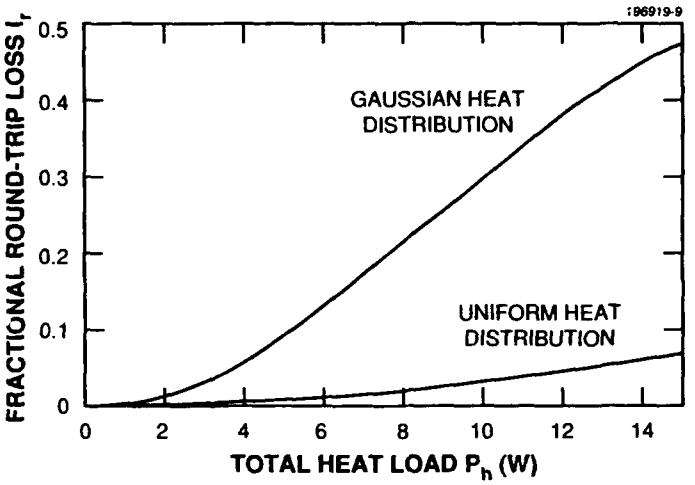

Figure 2-2. Fractional round-trip loss as a function of total heat load for uniform 1.06-μm illumination. The upper curve shows the case for heating by a Gaussian beam with R = 1 cm, L = 0.1 cm, and ω_p = 0.1 cm. The lower curve is for a uniform heat distribution. In this example, P_h = 15 W approximately corresponds to the maximum stress that the crystal can endure before fracturing.

Uniform illumination of the disk is one way of approximating a multimode laser beam. Figure 2-2 shows the fractional round-trip loss for uniform laser illumination and for heating by a Gaussian beam with R = 1 cm, L = 0.1 cm, and ω_p = 0.1 cm. Also shown in Figure 2-2 is the fractional loss associated with a uniform heat distribution. In this example, P_h = 15 W approximately corresponds to the maximum stress that the crystal can withstand before fracturing. Comparison of the two curves shows that stress-induced birefringence causes much larger losses when the heat is concentrated in a small region as is the case for a Gaussian distribution.

K. F. Wall

REFERENCES

1. W. Koechner, *Appl. Opt.* **9**, 1429 (1970).
2. Solid State Research Report, MIT Lincoln Laboratory, 1991:4, p. 25
3. W. Koechner and D. K. Rice, *IEEE J. Quantum Electron.* **QE-6**, 557 (1970).
4. J. D. Foster and L. M. Osterink, *J. Appl. Phys.* **41**, 3656 (1970).
5. M. A. Karr, *J. Appl. Opt.* **10**, 893 (1971).

3. MATERIALS RESEARCH

3.1 MULTIPLE-QUANTUM-WELL GaInAsSb/AlGaAsSb DIODE LASERS EMITTING AT 2.1 μm

High-performance diode lasers emitting between 2 and 5 μm would be very useful for applications such as laser radar exploiting atmospheric transmission windows, remote sensing of atmospheric gases, molecular spectroscopy, and laser medicine. Lasers that incorporate a double heterostructure (DH) consisting of a GaInAsSb active layer and AlGaAsSb confining layers have shown good performance [1],[2], because this structure can provide the high level of electrical and optical confinement necessary for efficient laser operation. We have previously reported the pulsed room-temperature operation of such lasers emitting between 2.1 and 2.3 μm with differential quantum efficiency η_d as high as 50% [1], output power as high as 900 mW/facet [1], and threshold current density J_{th} as low as 940 A/cm^2 [2]. In addition, CW operation was obtained up to 30°C, with output powers up to 10.5 and 4.5 mW/facet at heatsink temperatures of 5 and 20°C, respectively [2]. Until now, these have been the best values reported for diode lasers emitting beyond 2 μm. We have also reported InAsSb/AlAsSb DH lasers emitting at 4.0 μm with CW operation up to 80 K and pulsed operation up to 155 K [3].

We have now demonstrated the first GaInAsSb/AlGaAsSb diode lasers with a quantum-well active region. The performance of these lasers, which emit at ~ 2.1 μm, is greatly superior to the performance of our DH devices emitting between 2.1 and 2.3 μm. Output power up to 190 mW/facet has been achieved for CW operation at a heatsink temperature of 20°C.

The following layers were grown on an n-GaSb substrate by molecular beam epitaxy: n^+-GaSb buffer, 2.0-μm-thick n-$Al_{0.9}Ga_{0.1}As_{0.07}Sb_{0.93}$ cladding, active consisting of five 10-nm-thick $Ga_{0.84}In_{0.16}As_{0.14}Sb_{0.86}$ wells and 20-nm-thick $Al_{0.2}Ga_{0.8}As_{0.02}Sb_{0.98}$ barriers, 2.0-μm-thick p-$Al_{0.9}Ga_{0.1}As_{0.07}Sb_{0.93}$ cladding, and 0.05-μm-thick p^+-GaSb contacting. All the layers are nominally lattice matched to the substrate. The growth and properties of GaSb-based alloys have been described previously [4]. Broad-stripe lasers 100 μm wide were fabricated using a lift-off process reported earlier, in which the p^+-GaSb layer is etched off the area between the stripes [1].

The emission spectra of the multiple-quantum-well (MQW) lasers show multiple longitudinal modes with full width at half-maximum of ~ 5 nm. As the cavity length L is decreased from 1000 to 300 μm, the peak emission wavelength at room temperature decreases from 2.14 to 2.11 μm as a result of band filling. For a given device, the wavelength increases with temperature at a rate of ~ 1.1 nm/°C because of the decrease in GaInAsSb bandgap.

In Figure 3-1, J_{th} for room-temperature pulsed operation is plotted vs $1/L$. As L is increased from 300 to 2000 μm, J_{th} decreases from 630 to 260 A/cm^2. These values are 2 to 3 times lower than those obtained for our best GaInAsSb/AlGaAsSb DH lasers [2]. The MQW values also compare favorably with those obtained for InGaAs/InGaAsP strained quantum-well lasers emitting at ~ 1.5 μm. The lowest J_{th} values obtained for the InGaAs/InGaAsP lasers are 160 A/cm^2 for a single quantum well [5] and ~ 400 A/cm^2 for four quantum wells [5],[6].

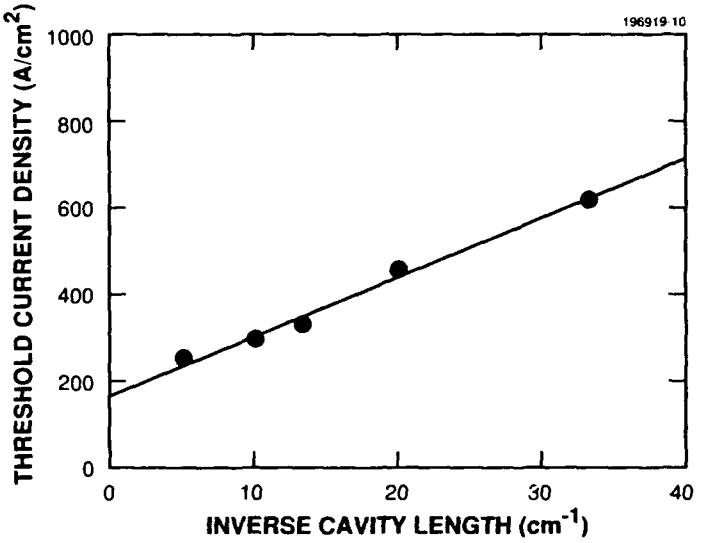

Figure 3-1. Room-temperature pulsed threshold current density vs inverse cavity length for 100-μm-wide GaInAsSb/AlGaAsSb MQW lasers.

Figure 3-2 shows J_{th} vs heatsink temperature for pulsed operation up to 150°C of an MQW laser 1000 μm long. Near room temperature the characteristic temperature T_0 is 113 K, compared with ~ 50 K for DH lasers [1],[2]. The marked increase in T_0 indicates that losses due to Auger recombination are substantially reduced in the quantum-well devices. At temperatures higher than 100°C, however, T_0 decreases to 45 K, probably because of the increase in Auger recombination with increasing temperature. The dramatic improvement in the room-temperature T_0 value for GaInAsSb/AlGaAsSb MQW lasers relative to DH devices is in marked contrast with the results for InGaAs/InGaAsP lasers. For both DH and quantum-well InGaAs/InGaAsP devices, the T_0 values are ~ 50 K [7], except for one report [5] of T_0 as high as 97 K for MQW lasers.

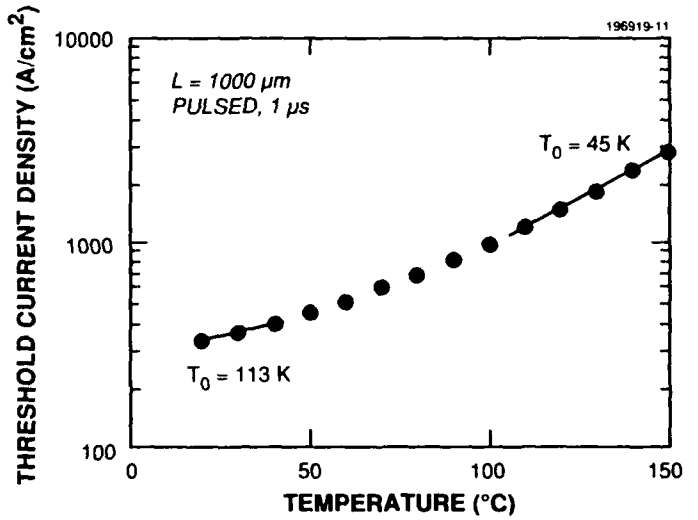

Figure 3-2. Pulsed threshold current density vs heatsink temperature for a 1000-μm-long GaInAsSb/AlGaAsSb MQW laser.

Figure 3-3 shows a plot of η_d^{-1} as a function of L. The highest value of η_d is 70% for $L = 300\ \mu m$. From the intercept and slope of the straight line fitted to the data the internal quantum efficiency is ~ 87%, and the internal loss coefficient α is ~ 10 cm^{-1} compared with 43 cm^{-1} obtained for DH lasers [2]. The substantial reduction in α results from a decrease in optical confinement in the thinner MQW active layers because the absorption in the cladding is smaller than in the active layers.

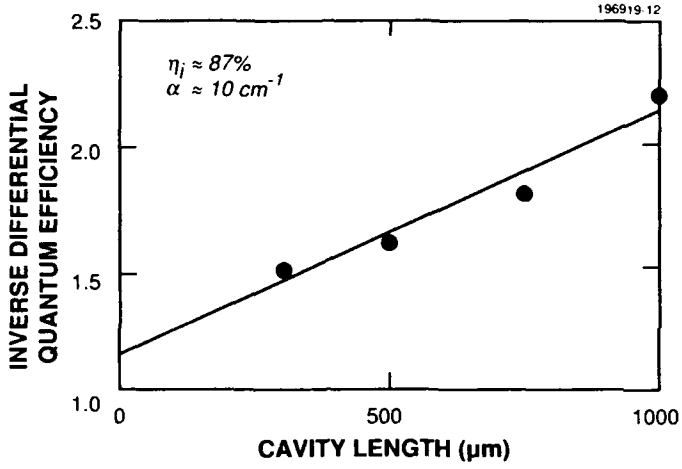

Figure 3-3. Inverse differential quantum efficiency vs cavity length for 100-μm-wide GaInAsSb/AlGaAsSb MQW lasers.

Lasers with a silicon-nitride-defined stripe 100 μm wide were fabricated for CW operation. Because of current spreading in the p^+ contacting layer below the silicon nitride, the pulsed J_{th} values were about 50% higher than those shown in Figure 3-1 for mesa-stripe devices. Several devices 1000 μm long have been mounted junction side down on copper heatsinks using In solder. Figure 3-4 shows the output power vs current curve for a device operated at a heatsink temperature of 20°C. The threshold current is ~ 570 mA, and the initial slope efficiency is ~ 0.1 W/A per facet. The maximum output power is 190 mW/facet, limited by the junction temperature rise. Another device, whose facets are coated with 10-nm-thick aluminum oxide, is being lifetested at a heatsink temperature of 20°C. No appreciable degradation has been observed over more than 300 h of operation at a CW output power of 90 mW/facet.

These GaInAsSb/AlGaAsSb quantum-well lasers show a dramatic improvement in performance over DH lasers, and optimization of the MQW structure can be expected to result in further improvement. Incorporation of strained quantum wells, which can easily be accomplished by changing the compositions of the GaInAsSb wells and AlGaAsSb barriers, may also lead to improved performance, in view of the marked superiority of strained-layer InGaAs/AlGaAs and InGaAs/InGaAsP quantum-well lasers over lattice-matched devices.

H. K. Choi
S. J. Eglash

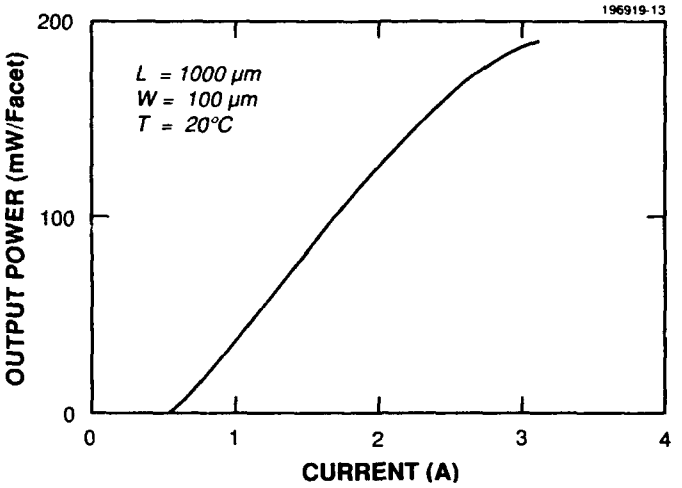

Figure 3-4. Output power vs current for CW operation of a 100-μm-wide by 1000-μm-long GaInAsSb/AlGaAsSb MQW laser.

3.2 IMPROVEMENT IN INFRARED FOCAL PLANE ARRAY SENSITIVITY BY USING MONOLITHIC Si MICROLENS ARRAYS

The most highly developed technology currently available for large-area staring infrared (IR) focal plane arrays (FPAs) utilizes silicide Schottky-barrier detectors [8], even though these internal-photoemission detectors have much lower quantum efficiencies than detectors based on interband absorption in semiconductors such as HgCdTe and InSb. The advantage of the silicide detectors is that they are fabricated on Si substrates by standard integrated circuit processing techniques. Therefore, it is possible to manufacture large, highly uniform arrays of detectors that are monolithically integrated with low-noise Si readout circuitry. However, the usual monolithic approach has the significant drawback of a reduced detector fill factor, since some fraction of the pixel area must be used for readout. Typical fill factors are 30 to 50% for arrays with CCD readout. The fill factor and therefore the FPA sensitivity can be improved by using a microscopic lens array to redirect the incident radiation onto the detectors. Various microlens configurations have been proposed, including complex diffractive gratings [9] and miniature refractive elements [10]. Improvement in sensitivity has been demonstrated by Erhardt et al. [11], who used a hybrid cylindrical lens array mechanically attached to a 32 × 63-element PtSi array with a fairly large pixel size of 80 × 160 μm.

We are developing monolithic two-dimensional arrays of quasispherical Si microlenses that are etched directly into the back side of back-illuminated FPAs. As shown schematically in Figure 3-5, each microlens, which is in registration with an individual pixel, serves as a reimaging field lens between the primary objective lens and the FPA. If the f-number of the field lens is properly designed, almost all incoming IR radiation can be collected by the detector, resulting in a fill factor approaching 100%. Figures 3-6(a) and 3-6(b) show perspective and cross-sectional views, respectively, of an etched microlens array with a 40-μm pitch. Over a large area the microlenses have very smooth surface morphology and extremely uniform dimensions. As an initial demonstration of the monolithic microlens technology, we have fabricated 320 × 244-element PtSi Schottky-barrier FPAs with microlens arrays formed at the top and center. Since the f-number of the primary

objective is 2.35, the microlens f-number is designed to be 1.3, so that most of the radiation incident on each 40-μm-wide pixel is focused onto the 23.5-μm-wide detector. Figure 3-7(a) shows an uncorrected medium-wavelength IR image of a man's hand. The regions of the FPA with microlens arrays are seen to have higher responsivity than the regions without these arrays, as shown by the increase in both background and signature signals. The FPA sensitivity is increased by 50 to 60%. The background-subtracted image is shown in Figure 3-7(b).

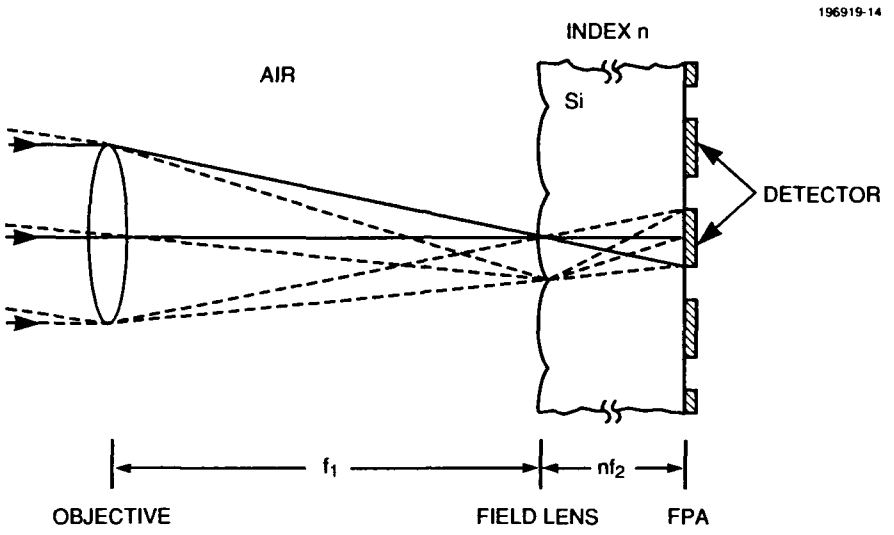

Figure 3-5. Schematic diagram showing a monolithic Si microlens array fabricated on back side of FPA for increasing detector fill factor and array sensitivity.

In addition to increasing FPA sensitivity for the present detector geometry, microlens arrays would allow the detector area to be further reduced without sacrificing sensitivity, provided that all the incident radiation was still collected. A reduction in detector area would have several benefits. First, it would lead to a lower dark current and therefore permit higher operating temperatures. Second, it should improve FPA radiation hardness by decreasing the collection volume for radiation-induced charge. Finally, it would permit additional circuitry to be included on the focal plane, even within the pixels, to achieve on-plane signal processing.

B-Y. Tsaur C. K. Chen
A. H. Loomis S. A. Marino

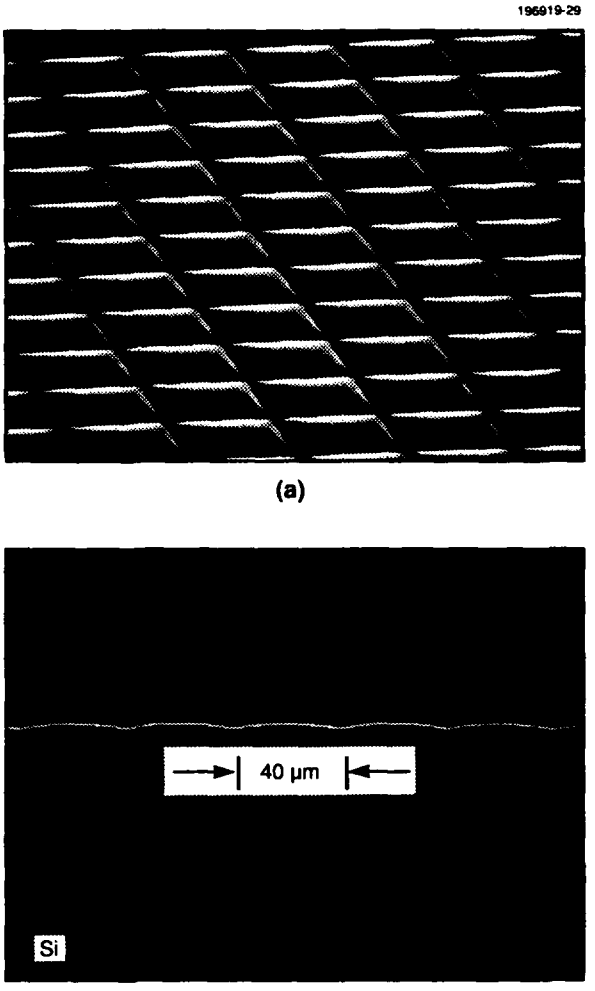

Figure 3-6. Photomicrographs showing (a) top and (b) cross-sectional views of a monolithic Si microlens array fabricated on back side of FPA.

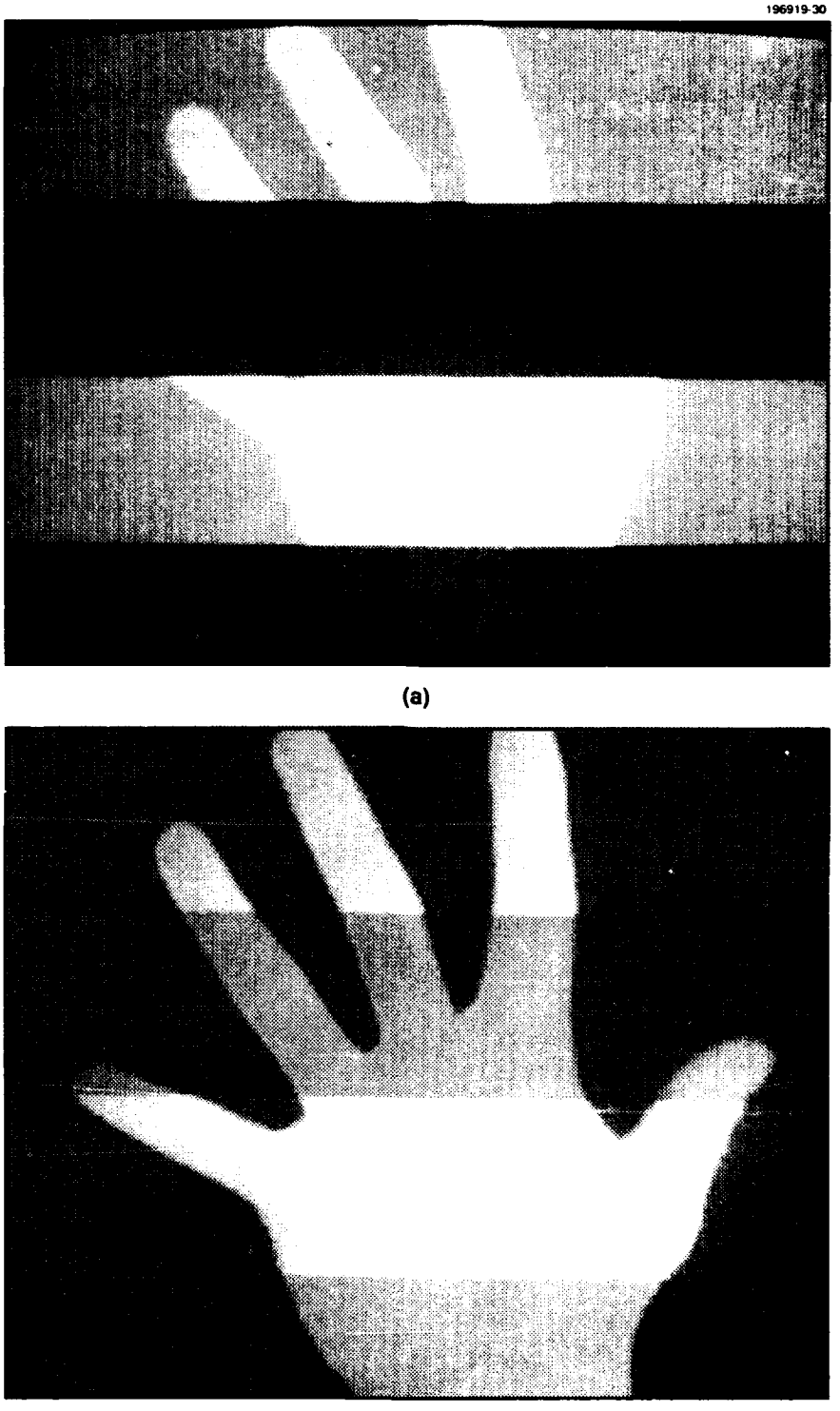

Figure 3-7. (a) Uncorrected medium-wavelength IR image of a man's hand obtained from a PtSi array with Si microlens arrays fabricated on the top and middle regions. (b) Background-subtracted image of (a).

3.3 OMVPE REGROWTH OF CH_3I-VAPOR-ETCHED GaAs

In several studies [12]-[16], vapor etching of III-V compound semiconductors has been investigated as a possible method for in situ surface treatment permitting the vapor growth of epilayers with improved surface morphology and electrical characteristics. In situ vapor etching following conventional wet chemical substrate cleaning has been shown to reduce impurity accumulation at the epilayer-substrate interface [12],[14],[16]. For the fabrication of numerous advanced microwave and optoelectronic device structures, in situ etching of growth-interrupted and photolithographically processed epilayer surfaces is crucial for obtaining high-quality regrowth. For the vapor etchants studied previously, however, the etching temperatures required to maintain a featureless surface morphology are quite high (> 750°C). Such temperatures can result in dopant and/or alloy interdiffusion that degrades device performance.

We have recently reported the vapor etching of GaAs substrates with an alternative etchant, CH_3I, that is liquid at room temperature, has a suitable vapor pressure, and is noncorrosive [17]. This etchant should therefore be compatible with organometallic vapor phase epitaxy (OMVPE) systems. Featureless surface morphology can be maintained with this etchant at temperatures of only 450 to 500°C. The etch rate is controlled by gas phase processes, suggesting that spatially uniform etch rates could be obtained in OMVPE reactors to yield uniform epilayers. This etchant should therefore be of great interest for use in conjunction with OMVPE growth for the fabrication of optoelectronic integrated circuits (OEICs) and three-dimensional integrated structures.

As a further step in the development of in situ CH_3I etching technology, we have now performed a series of GaAs growth interruption experiments. In each group of experiments, a nominally undoped GaAs epilayer 2 μm thick was first grown at 700°C on a GaAs substrate wafer in a vertical rotating-disk OMVPE reactor [18]. The wafer was removed from the reactor and cleaved into several test samples. A test sample was transferred to a separate horizontal reactor for etching with CH_3I vapor in H_2 carrier gas, and a control sample was loaded into the OMVPE reactor. The test sample was vapor etched with CH_3I and then transferred to the OMVPE reactor. All test and control samples were briefly exposed to air (< 1 min) prior to their loading into the OMVPE reactor for regrowth of a 1-μm-thick second epilayer under the same conditions used for the first growth. Regrowth experiments were performed on test samples that were etched with CH_3I under various conditions, and also on samples that had the first epilayer treated by a 1-min H_2SO_4 dip followed by an 18-MΩ deionized water rinse.

Figure 3-8 shows the profile of carrier concentration vs depth obtained by capacitance-voltage measurements on a control sample for which the first epilayer was exposed to air before growth of the second epilayer. The profile exhibits a peak due to electron accumulation at the regrowth interface between the two epilayers. The net electron accumulation is 1.7×10^{11} cm^{-2}. Measurements on other control samples gave similar profiles with accumulations ranging up to 2.3×10^{11} cm^{-2}.

In one set of experiments, a second epilayer was grown on samples with first epilayers that had been vapor etched at 500°C for 15 min with CH_3I concentrations of 1.5, 2.25, and 3×10^{-2} mole fraction. The thickness of GaAs removed increased from 0.22 μm at the lowest concentration to 0.35 μm at the highest. The carrier concentration depth profiles were similar to the profiles for the control samples. Figure 3-9 shows the net electron accumulation at the regrowth interface as a function of CH_3I concentration. The accumulation range is 2.1 to 2.7×10^{11} cm^{-2}, only slightly higher than the values for the control samples.

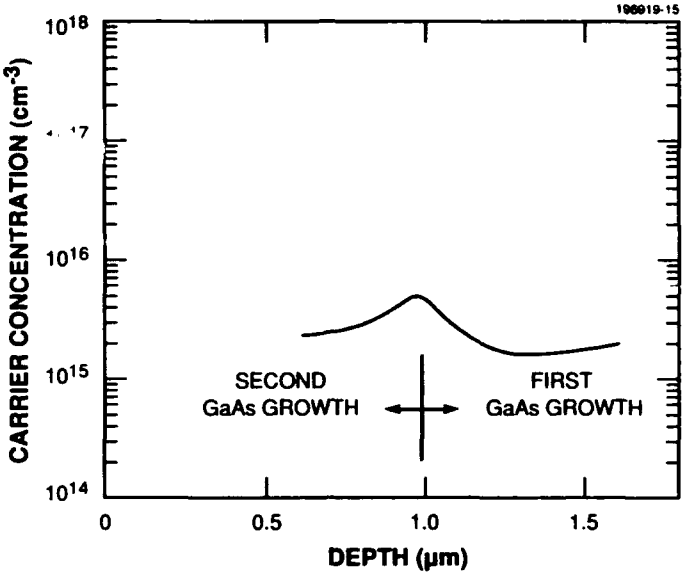

Figure 3-8. Carrier concentration vs depth for a GaAs regrowth sample in which the first epilayer was untreated.

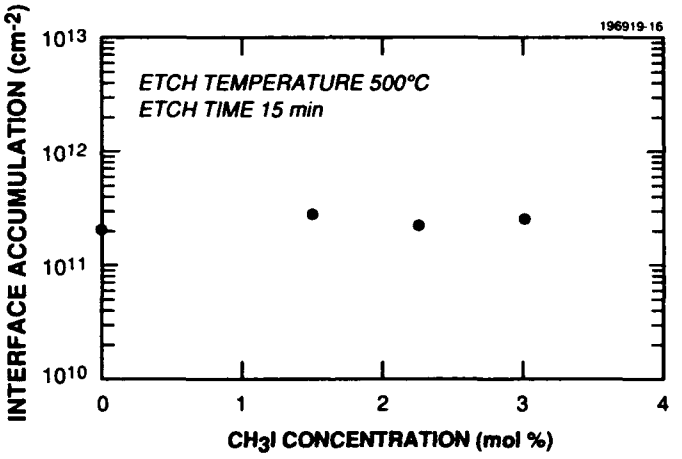

Figure 3-9. Effect of CH_3I concentration on electron accumulation at the regrowth interface.

In other experiments, regrowth was performed on samples with first epilayers that had been etched with CH_3I at a concentration of 1.5×10^{-2} mole fraction for 15 or 30 min at four temperatures from 460 to 520°C. The thickness removed by etching for 15 min increased from 0.05 μm at 460°C to 0.44 μm at 520°C. The surface morphology of the second epilayer was specular for all samples. Figure 3-10 shows Nomarski interference contrast micrographs obtained after regrowth for samples etched for 15 min. No texture is observed for the samples etched at 460 and 480°C, but those etched at 500 and 520°C show increasing texture. Figure 3-11 illustrates the net electron accumulation at the regrowth interface as a function of etching temperature. The accumulation is insensitive to etching temperature and time, ranging from 2.1 to 2.7 ×

10^{11} cm^{-2} for an etching time of 15 min and from 2.4 to 2.9 × 10^{11} cm^{-2} for a time of 30 min. The highest of these values is about 25% higher than the highest of the control values.

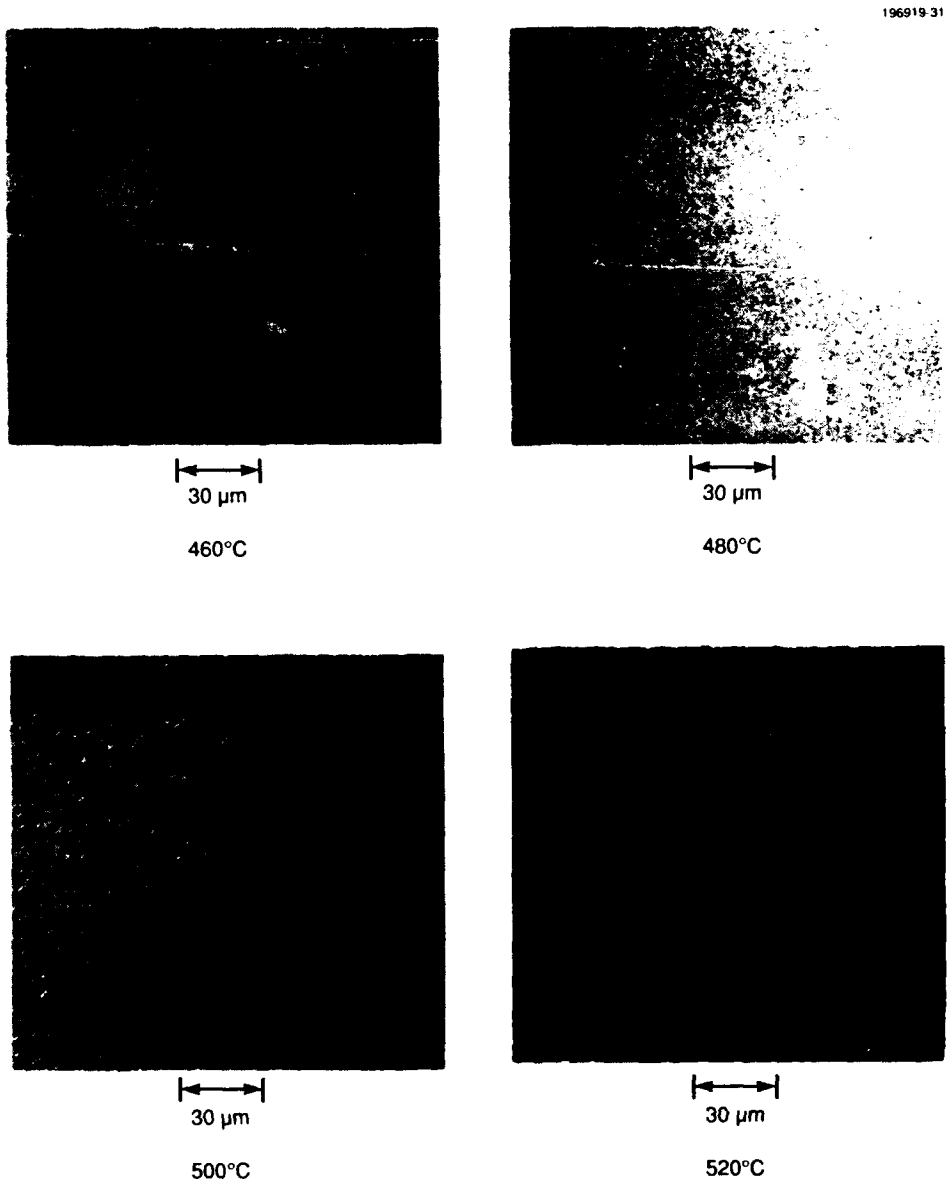

Figure 3-10. Surface morphology of regrowth samples with first epilayers etched with CH_3I at temperatures of 460, 480, 500, and 520°C.

The optical quality of regrown GaAs samples was characterized by photoluminescence (PL) measurements at 4 K. Figure 3-12 shows the spectra for an untreated control sample and for a sample that had the first epilayer etched with CH_3I at 460°C for 15 min. The PL intensity is slightly lower for the etched sample, but the relative intensities of the peaks due to the bound exciton and carbon acceptor are similar.

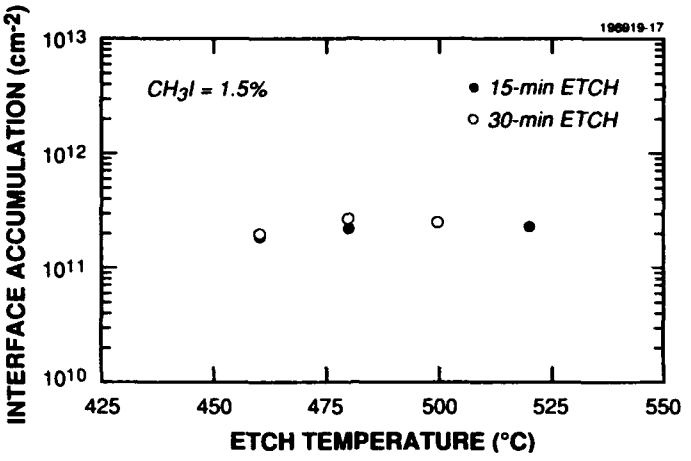

Figure 3-11. Effect of CH_3I etch temperature and time on electron accumulation at the regrowth interface.

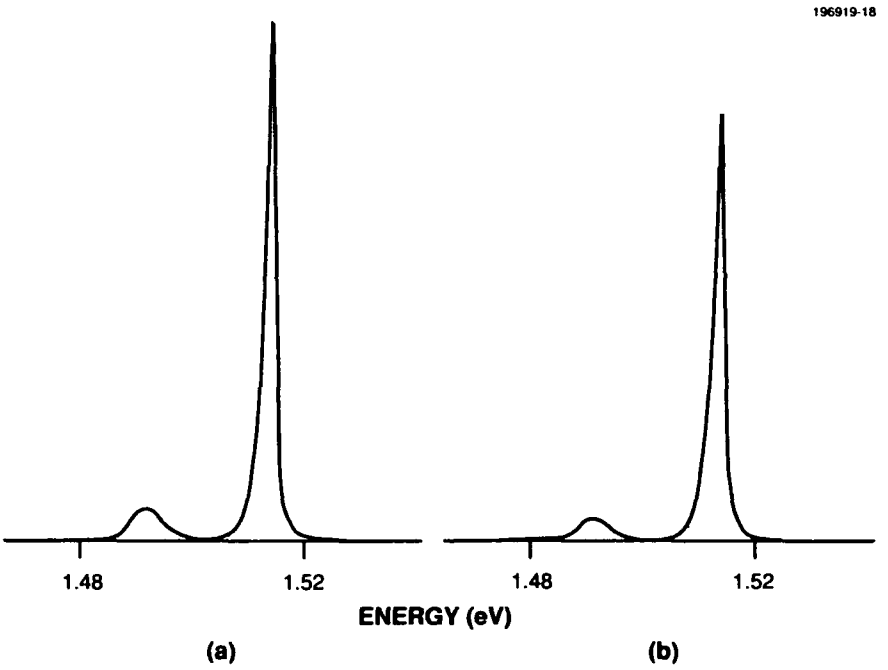

Figure 3-12. Photoluminescence of GaAs regrowth samples (a) with no surface treatment and (b) with 82.5 nm removed by CH_3I etching at 460°C.

In a study of the OMVPE growth of GaAs epilayers on GaAs substrates [16], it was found that the electron accumulation at the epilayer-substrate interface was significantly increased by pregrowth treatment of the substrate with H_2SO_4. We have found that this effect can be overcome by CH_3I etching. An H_2SO_4 dip was used to treat the first epilayer on two samples from the same wafer. One sample was then etched at 480°C for 15 min with CH_3I at a concentration of 1.5×10^{-2} mole fraction to remove 0.1 μm, after which a second

epilayer was grown simultaneously on both samples. Figure 3-13 shows the profiles of carrier concentration vs depth for the two samples. The net electron accumulation at the regrowth interface was 5.2×10^{11} cm^{-2} for the sample that was not etched with CH_3I. Etching with CH_3I was successful in reducing the accumulation to 2.9×10^{11} cm^{-2}, not much higher than the value of 2.5×10^{11} cm^{-2} obtained for the previous sample that had been etched with CH_3I under the same conditions but not treated with H_2SO_4.

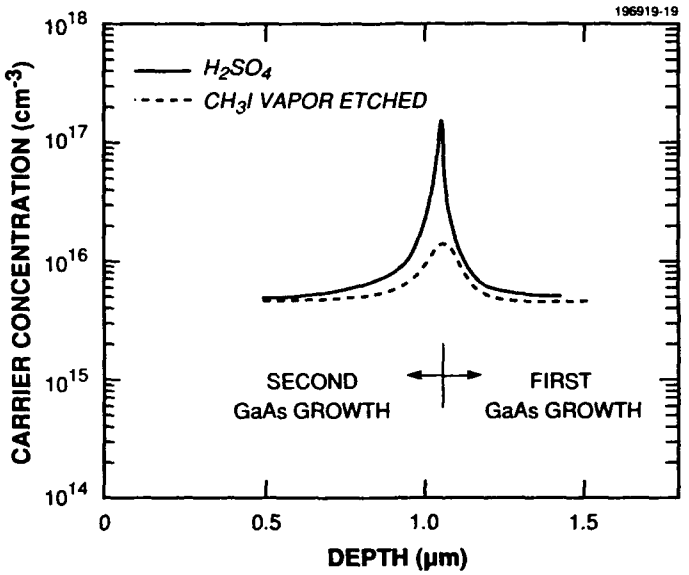

Figure 3-13. Carrier concentration vs depth for H_2SO_4-treated samples with and without CH_3I etching.

In conclusion, a second GaAs epilayer has been grown by OMVPE on first epilayers that were either untreated or etched ex situ with CH_3I vapor and/or H_2SO_4. For CH_3I etch temperatures below 500°C, the surface morphology and low-temperature PL are comparable for epilayers grown on CH_3I-etched and untreated first epilayers. Carrier concentration depth profiles show that CH_3I etching introduces very little electron accumulation at the regrowth interface and eliminates most of the electron accumulation resulting from H_2SO_4 etching. If similar results can be obtained for AlGaAs epilayers, in situ CH_3I etching should become an extremely useful technique in conjunction with OMVPE for the fabrication of complex structures such as OEICs and three-dimensional integrated structures.

C. A. Wang
C. W. Krueger
M. Flytzani-Stephanopoulos*
R. A. Brown*

*Author not at Lincoln Laboratory.

REFERENCES

1. H. K. Choi and S. J. Eglash, *IEEE J. Quantum Electron.* **27**, 1555 (1991), and references therein.
2. H. K. Choi and S. J. Eglash, *Appl. Phys. Lett.* **59**, 1165 (1991).
3. H. K. Choi and S. J. Eglash, presented at IEEE Lasers and Electro-Optics Soc. Ann. Mtg., San Jose, Calif., 4-7 November 1991, Paper SDL 6.2.
4. S. J. Eglash and H. K. Choi, in *Gallium Arsenide and Related Compounds 1991*, G. B. Stringfellow, ed. (IOP Publishing, Bristol, England, 1992).
5. P. J. A. Thijs, L. F. Tiemeijer, P. I. Kuindersma, J. J. M. Binsma, and T. Van Dongen, *IEEE J. Quantum Electron.* **27**, 1426 (1991).
6. W. T. Tsang, F. S. Choa, M. C. Wu, Y. K. Chen, A. M. Sergent, and P. F. Sciortino, *Appl. Phys. Lett.* **58**, 2610 (1991).
7. W. T. Tsang, F. S. Choa, R. A. Logan, T. Tanbun-Ek, A. M. Sergent, and K. W. Wecht, *Appl. Phys. Lett.* **60**, 18 (1992), and references therein.
8. F. D. Shepherd and A. C. Yang, *Int. Electron Devices Mtg. Tech. Dig.* (IEEE, New York, 1973), p. 310.
9. T. A. Fritz and J. A. Cox, *Proc. SPIE* **1052**, 25 (1989).
10. E. F. Cross, W. A. Garber, G. D. Wiemokly, O. L. Gibb, and I. J. Spiro, *Proc. SPIE* **366**, 10 (1982).
11. H. G. Erhardt, J. Kane, and L. S. O'Hara, *Proc. SPIE* **501**, 165 (1984).
12. R. Bhat and S. K. Ghandhi, *J. Electrochem. Soc.* **125**, 771 (1978).
13. M. Heyen and P. Balk, *J. Cryst. Growth* **53**, 558 (1981).
14. B. El Jani, M. Guittard, J. C. Grenet, and P. Gibart, *J. Cryst. Growth* **60**, 131 (1982).
15. A. R. Clawson, *J. Cryst. Growth* **69**, 346 (1984).
16. T. F. Kuech, E. Marshall, G. J. Scilla, R. Potemski, C. M. Ransom, and M. Y. Hung, *J. Cryst. Growth* **77**, 539 (1986).
17. C. W. Krueger, C. A. Wang, and M. Flytzani-Stephanopoulos, *Appl. Phys. Lett.* **60**, 1459 (1992).
18. C. A. Wang, S. Patnaik, J. W. Caunt, and R. A. Brown, *J. Cryst. Growth* **93**, 228 (1988).

4. SUBMICROMETER TECHNOLOGY

4.1 EFFECTS OF LINEWIDTH VARIATIONS ON THE SPATIAL MODES OF A CONCENTRIC-CIRCLE-GRATING SURFACE-EMITTING SEMICONDUCTOR LASER

A semiconductor laser operated in either the distributed feedback or distributed Bragg reflector configuration with a circularly symmetric grating will potentially produce a circularly symmetric output beam, with a relatively narrow frequency spectrum, from a larger emission area than that of more conventional semiconductor lasers. These points have been addressed in several recent theoretical papers [1]-[5]. In addition, one recent experimental paper reports surface emission and lasing in an optically pumped, double-heterostructure InGaAsP/InP laser that contained an electron-beam-written circular grating of period Λ = 0.397 μm (lasing wavelength $\lambda \approx 1.28$ μm) and overall diameter D = 280 μm [6]. The spatial modes of a concentric-circle-grating surface-emitting semiconductor laser are of central importance. High-quality circular gratings are needed if the laser is to support the desired radially inward- and outward-going circular waves, so it is important to assess both the grating quality that can be achieved using state-of-the-art fabrication processes and the impact of such gratings on laser operation.

Circular gratings of period $\Lambda = 0.25$ μm have been defined by electron-beam lithography using a JEOL JBX-5DII vector-scan system. Figure 4-1 shows a scanning electron micrograph (SEM) of a typical circular grating with a period $\Lambda = 0.25$ μm. Although it is impractical to scan a true circle with this electron-beam system, such features can be approximated using polygons comprising single-pass straight-line segments. Single-pass lines may be placed at arbitrary angles, a unique feature of the JEOL electron-beam writer. In this application, each electron-beam-defined ring was written as four overlapping polygons to improve the approximation. End points of the line segments are placed to provide an even exposure and are randomized in order to avoid angular correlations in the pattern data. The electron beam was accelerated by a 50-keV potential and yielded a line dose between 0.7 and 1.8 nC/cm. The resist consisted of 150 nm of poly(methyl methacrylate). After exposure and development, the grating pattern was etched into the upper cladding region of a graded-index separate-confinement heterostructure quantum-well laser structure using chemically assisted (chlorine) ion-beam etching. The undoped epilayers of the laser consisted of a 1.5-μm $Al_{0.85}Ga_{0.15}As$ lower cladding, a 0.3-μm parabolically graded region with a 10-nm GaAs quantum well, and 0.25-μm $Al_{0.85}Ga_{0.15}As$ upper cladding. The thin upper cladding layer enabled the TE_0 guided mode to couple very strongly to the grating at the air interface.

The lasers were mounted on heatsinks held at ~ 77 K and optically pumped by the 514.5-nm line of a CW argon-ion laser. Lasers with circular gratings varying in diameter from 80 μm (160 rings) to 500 μm (1000 rings) were fabricated. The focused pump beam (spot diameter of 80 μm) illuminated the center of the grating for this laser. The threshold pump power was P_{th} = 250 mW, corresponding to an intensity I_{th} = 4.5 kW/cm^2. We have measured thresholds as low as P_{th} = 30 mW (I_{th} = 540 W/cm^2) in devices with 0.25-μm-deep gratings. The observed spatial mode patterns are not circular but correspond to the x- and y-axes of the Cartesian pixel grid used by the electron-beam system in writing the grating. Just above threshold, lasing occurs only along the y-axis direction. Well above threshold, lasing also takes place along the x-axis direction and along axes

oriented at 45° with respect to the x- and y-axes. In all cases the light is polarized azimuthally, indicating lasing in the TE_0 guided mode. At no pump power does lasing occur along the remaining axial orientations.

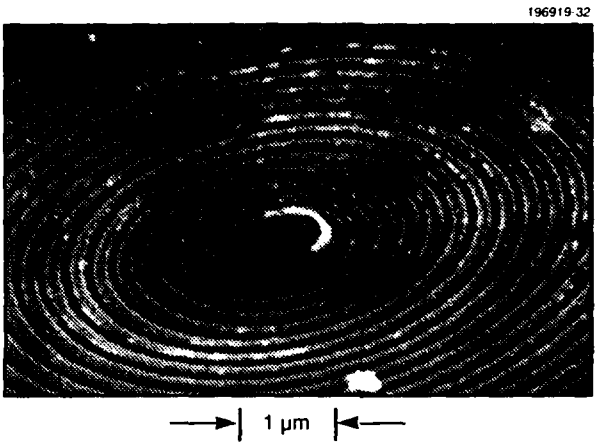

Figure 4-1. Scanning electron micrograph of the center portion of a 500-μm-diam, 0.25-μm-period grating fabricated by electron-beam lithography.

The near-field spatial mode patterns indicate an azimuthal variation of grating coupling strength, or reflectivity, around the circular grating. A careful optical inspection of the grating shows that the azimuthal grating uniformity is interrupted regularly in 9° increments, a feature not readily apparent in Figure 4-1. The nature of this azimuthal nonuniformity is shown schematically in Figure 4-2, in which the linewidth of the grating rings varies among the individual, uniform 9° wedge sections. Angled lines are defined by the electron-beam hardware by exposing points on a Cartesian grid. Because the density of points varies with angle, the electron-beam dose must also be varied in order to maintain a constant linewidth. The JEOL system tries to compensate for this effect by adding a constant dose correction to each 9° wedge section, but the corrections built into the JEOL software overcompensate, resulting in slightly wider linewidths in some wedge sections. These corrections can, in principle, be improved to give a more constant linewidth, but our application is among the first to reveal the consequences of these coarse corrections in such a striking fashion.

The variation in linewidth can be measured in high-magnification SEM images, and the variation in each quadrant of the circle is the same and is symmetric about the 45° axis of the quadrant. We have measured the linewidth a at various points along three directions in a 45° section; the dimensionless ratios a/Λ appear in Table 4-1, where 0° denotes either the x- or y-axis direction. Table 4-1 also lists both the relative decrease in coupling constant $\Delta\kappa = [\kappa(\theta) - \kappa(0)]/\kappa(0)$ as calculated from approximate analytical formulas for κ for a second-order rectangular grating [7], and the associated increase in the threshold gain α corresponding to the variation in a/Λ [8]. The results show that while the threshold gain α for lasing along the 45° direction is only ~ 3% higher than that along 0°, α for lasing along the 22.5° direction can be as much as 30% higher than that along 0°, indicating strong directional discrimination in the laser. These results suggest that for circular mode operation, for which lasing must occur along each diameter with similar α, the value of a/Λ should vary around

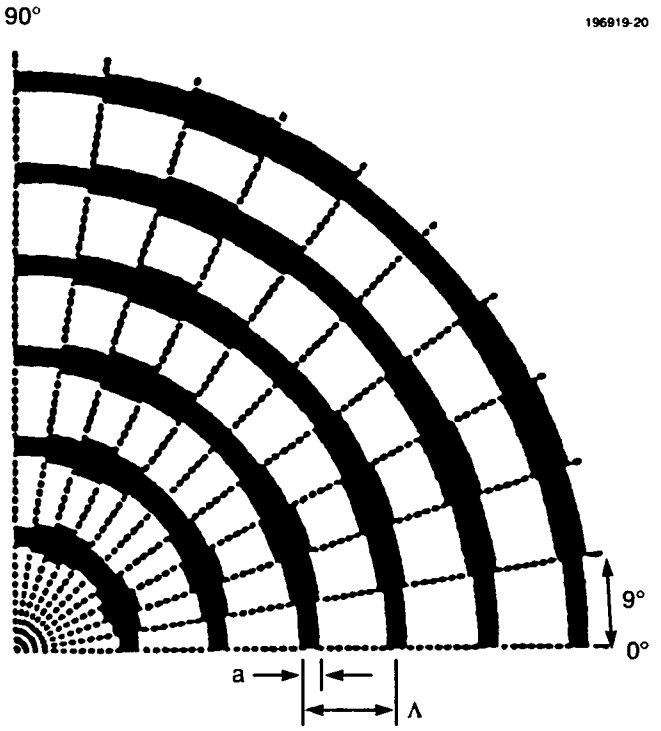

Figure 4-2. Exaggerated schematic illustration of six grating periods in one quadrant of a circular grating, demonstrating the variation of the linewidth a among the uniform 9° azimuthal increments.

TABLE 4-1

Measured Linewidths of Circular Grating Rings

Axis Angle (deg)	Measured Linewidth [a/Λ (±0.007)]	Δκ (%)	Δα (%)
0	0.329	0	0
22.5	0.369	−17	29
45	0.334	−1.7	2.7

the entire circle by an amount no greater than the measured difference between a/Λ for the 0° and 45° directions, since modes associated with these two directions are just barely able to lase simultaneously. For a safe estimate, a linewidth variation of less than ~ ±1%, corresponding to ~ ± 2% variation in α, is desirable.

C. L. Dennis
M. J. Rooks*
T. Erdogan*
O. King*
G. W. Wicks*
D. G. Hall*

*Author not at Lincoln Laboratory.

4.2 SELECTIVE-AREA GROWTH OF METAL OXIDE FILMS INDUCED BY PATTERNED EXCIMER LASER SURFACE PHOTOLYSIS

Selective-area oxide growth has been demonstrated as an all-dry surface-imaged resist process. The growth conditions result in oxide formation only on high-energy surfaces, so a surface energy increase induced by excimer laser irradiation of a low-energy surface can lead to selective growth. When a plasma-deposited hydrocarbon-based planarizing layer is chemically modified to exhibit low surface energy, the resulting selective oxide growth followed by oxygen plasma pattern transfer produces an all-dry lithographic process.

Low-energy surfaces have been prepared using either an RF barrel etcher or one of three RF parallel-plate reactive ion etchers. Discharges of SF_6, CF_4, CF_2Cl_2, or Cl_2 gas were employed. The resultant surfaces, when characterized by angle-dependent x-ray photoelectron spectroscopy and contact angle measurements, were similar in nature to the published results for the plasma fluorination of polymers [9]. Plasma-deposited planarization materials [10] were used for an all-dry process, and conventional spin-cast novolac polymers were also employed for convenience. The advancing contact angle with water of these surfaces ranged from 100° to 130°, indicating a critical surface tension [11] of 20 to 13 erg/cm^2, respectively. For the original novolac the contact angle was 90° and the surface energy was 31 erg/cm^2.

The reactants used are metal chlorides ($SiCl_4$, $GeCl_4$, and $SnCl_4$) and water. These metal chlorides will hydrolyze only with condensed phases of water. Experimentally, the growth is performed at temperatures from 5 to 15°C to provide rapid formation of physisorbed water layers. The H_2O and, for example, $SiCl_4$ are allowed into the chamber simultaneously at pressures of 1 to 10 Torr. The walls of the chamber are kept heated (55 to 65°C) to minimize growth on the chamber surfaces, and the growth is monitored using a quartz-crystal microbalance. For precise control of the oxide thickness, the reagents can be introduced sequentially via a molecular layer dosing technique [12], by which the oxide thickness can be controlled to within a few nanometers.

The growth on a hydrophilic surface has been studied in some detail in [13] and is correlated to the development of specific adsorbed H_2O phases. On a hydrophobic surface, where conformal adlayer formation does not occur, the onset of growth is limited by nucleation of molecular H_2O clusters. For patterning, the area selectivity of the growth process can be estimated from the thermodynamics of H_2O nucleation. Figure 4-3 shows relative thickness for growth on a hydrophobic surface compared to that on a hydrophilic (high-energy) surface. Plotting the data as relative thicknesses suppresses the appearance of growth-rate anomalies attributable to the experimental apparatus in which the gas pressures are cycled during growth. Note that, during the early stages of growth, the growth selectivity between the hydrophilic and hydrophobic (15 erg/cm^2) surfaces exceeds 10:1. The growth-rate induction is characteristic of delayed condensation and results from a thermodynamic nucleation barrier [14]. The existence of nucleation-limited growth is further supported by Figure 4-4, showing an electron micrograph of SiO_2 grown on a surface whose critical surface tension was 15 erg/cm^2, in which the nuclei are clearly visible. In contrast, growth of SiO_2 on high-energy surfaces results in conformal growth [13].

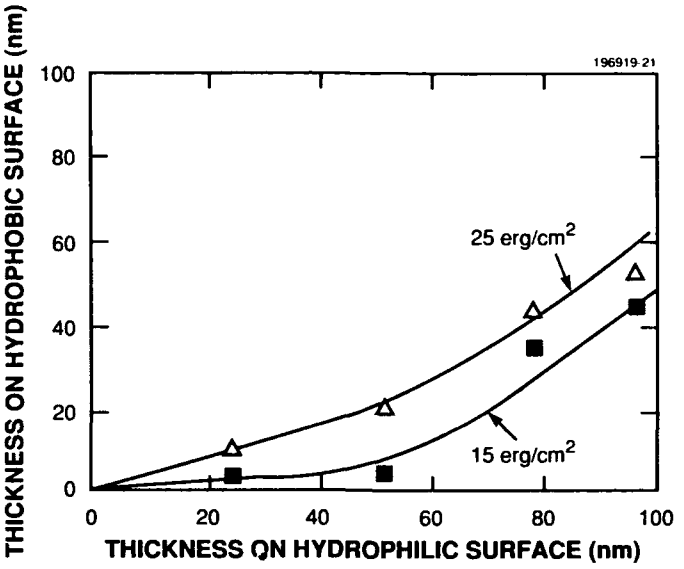

Figure 4-3. SiO_2 thicknesses grown on two hydrophobic (15 and 25 erg/cm^2) surfaces vs thickness grown on a hydrophilic SiO_2 (> 200 erg/cm^2) surface.

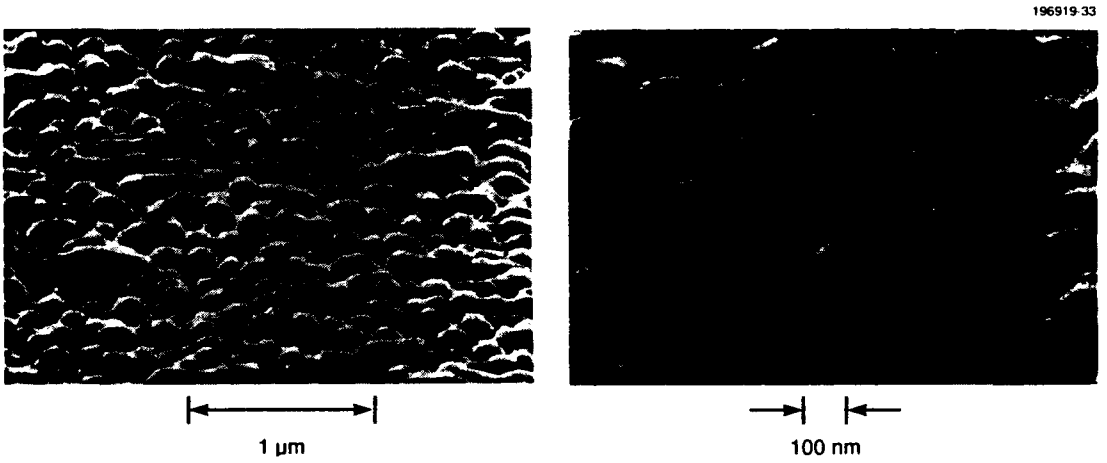

Figure 4-4. Surface morphology shown at two different magnifications for SiO_2 grown from $SiCl_4$ and H_2O on a 15-erg/cm^2 surface at a temperature of 13°C.

Understanding the H_2O nucleation behavior allows prediction of the ultimate growth selectivities. The H_2O nucleation rate I is given by [14]

$$I = kJ \sin\theta (G_{\text{nuc}})^{1/2} \exp\left[(G_{\text{des}} - G_{\text{diff}} - G_{\text{nuc}})/kT\right] , \tag{4.1}$$

where k is a constant, J is the molecular flux to the surface, θ is the contact angle, G_{des} is the activation energy for H_2O desorption, G_{diff} is the activation energy for H_2O surface diffusion, and G_{nuc} is the free energy change upon nucleation of a critically sized H_2O cluster. Changes in critical surface tension upon irradiation change θ, G_{des}, G_{diff}, and G_{nuc}. We have quantitatively calculated G_{nuc} using cluster radii derived from molecular dynamics calculations [15] and have found that it is only weakly dependent on surface energy and can be assumed constant. G_{diff} and G_{des} are coupled, and as a simplest estimate G_{diff} can be assumed equal to $G_{des}/2$, so the two terms can be combined. Apparently, it is the changes in contact angle together with changes in G_{des}, or more simply the H_2O desorption probability, that are modified upon irradiation. On the assumption that $G_{nuc} = 0.1$ eV, even small surface changes, such as G_{des} increasing from 0.2 to 0.4 eV/molecule and θ decreasing from 120° to 20°, will increase the nucleation rate by a factor of 24. These large increases in nucleation rate result in the growth becoming limited only by the molecular H_2O flux, and delayed growth due to a nucleation barrier does not occur. Transition to this growth regime is the central point to the selective growth process.

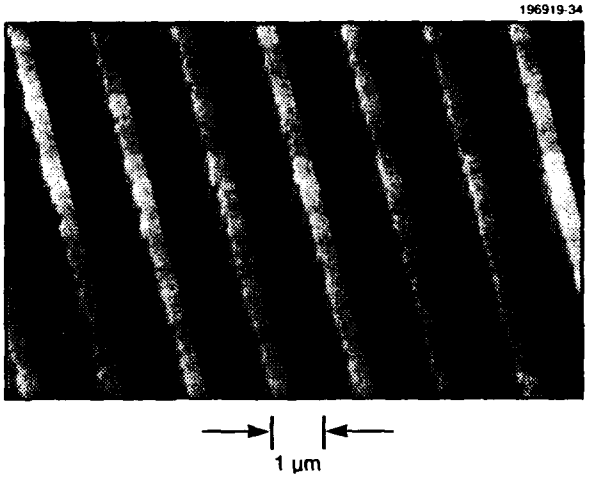

Figure 4-5. Lines of 0.5-µm thickness patterned by contact printing a CF_2Cl_2-modified novolac surface with 10 J/cm^2 at 193 nm. The total growth time was 2.5 min. After selective SiO_2 growth, the resultant features were produced by pattern transfer in an oxygen reactive ion etcher.

Patterning of a submicrometer image has been achieved and is shown in Figure 4-5. This sample was a CF_2Cl_2-treated novolac polymer contact printed at 193 nm using a dose of 10 J/cm^2. The high dose was necessary to ensure high growth selectivity. Other surfaces, such as chlorine-modified polymers, exhibited measurable but lower growth selectivity at doses as low as 200 mJ/cm^2.

R. R. Kunz J. Melngailis
D. J. Ehrlich M. W. Horn

REFERENCES

1. T. Erdogan and D. G. Hall, to be published in *IEEE J. Quantum Electron.*
2. C. Wu, T. Makino, J. Glinski, R. Maciejko, and S. I. Najafi, *IEEE J. Lightwave Technol.* **9**, 1264 (1991).
3. X. H. Zheng and S. Lacroix, *IEEE J. Lightwave Technol.* **8**, 1509 (1990).
4. T. Erdogan and D. G. Hall, *J. Appl. Phys.* **68**, 1435 (1990).
5. M. Toda, *IEEE J. Quantum Electron.* **26**, 473 (1990).
6. C. Wu, M. Svilans, M. Fallahi, T. Makino, J. Glinski, C. Maritan, and C. Blaauw, *Electron. Lett.* **27**, 1819 (1991).
7. W. Streifer, D. R. Scifres, and R. D. Burnham, *IEEE J. Quantum Electron.* **QE-11**, 867 (1975).
8. H. Kogelnik and C. V. Shank, *J. Appl. Phys.* **43**, 2327 (1972).
9. H. V. Boenig, *Fundamentals of Plasma Chemistry and Technology* (Technomic, Lancaster, Penn., 1988), Chap. 12.
10. S. W. Pang and M. W. Horn, *J. Vac. Sci. Technol. B* **8**, 1980 (1990).
11. W. A. Zisman, in *Contact Angle, Wettability, and Adhesion*, F. M. Fowkes, ed., Vol. 43 of *Advances in Chemistry Series* (American Chemical Society, Washington, D.C., 1964), p. 1.
12. D. J. Ehrlich and J. Melngailis, *Appl. Phys. Lett.* **58**, 2675 (1990).
13. N. Awaya and Y. Arita, *Jpn. J. Appl. Phys.* **25**, L24 (1986).
14. R. A. Sigsbee and G. M. Pound, *Adv. Coll. Int. Sci.* **1**, 335 (1967).
15. J. Hautman and M. L. Klein, *Phys. Rev. Lett.* **67**, 1763 (1991).

5. HIGH SPEED ELECTRONICS

5.1 FABRICATION AND PERFORMANCE OF MULTICELL POWER PBTs

Numerous applications exist for a transistor capable of highly efficient power generation up through K-band frequencies. The GaAs permeable base transistor (PBT), developed at Lincoln Laboratory, has demonstrated very promising performance as such a power transistor [1]-[3]. This section describes the fabrication and performance of new multicell PBT devices, and Section 5.2 reports the performance of 20-GHz power amplifiers fabricated using them.

Excellent power-added efficiencies of 66, 41, and 45% have been obtained from discrete PBT devices operating at 1.3, 20, and 22 GHz, respectively [2]. Although the power-added efficiency of discrete PBTs has been exceptional, the output power of the device has generally been suitable for only low- to medium-power applications. Therefore, we are developing a power PBT that utilizes chip-level power combining of several active-area PBT cells to increase the output power of the overall device. The new multicell PBTs described here consist of dual-cell and four-cell PBTs, where each cell has an active area of $8 \times 20\ \mu$m, thereby increasing the output power by approximately a factor of 2 and 4, respectively. These multicell devices represent a new type of PBT with significantly improved output power capability as well as high efficiency and compatibility with monolithic microwave integrated circuit technology.

A schematic of the dual-cell PBT structure is shown in Figure 5-1. The PBT is a vertical transistor in which the emitter and collector of the device are separated by a submicrometer-periodicity tungsten grating that forms the base of the transistor. This tungsten grating is embedded in the GaAs using organometallic chemical vapor deposition. For each active area two large tungsten pads that connect the base gratings are positioned such that one base pad rests on each side of the collector. Top-surface ohmic metal contacts are used to form the collector and emitter contacts. The emitter contact pads lie alongside the base pads and are interconnected with air bridges. All devices contain top-side base, collector, and emitter contacts, enabling each dual-cell device to be wafer probed. Details of the device fabrication are described in [4].

The four-cell PBT comprises two dual-cell devices combined in parallel, with a via-hole ground return located between the adjacent dual-cell structures. This configuration, shown in Figure 5-2, results in significantly improved gain and power-added efficiency over that which relies exclusively on air bridges for the RF ground return. A wafer thickness of 50 μm is used to minimize thermal resistance and inductance to ground. The smallest separation distance between active areas is 44 μm, which was determined to be sufficient to prevent the heating of an active area by adjacent active areas.

The dc current vs voltage curves for a dual-cell PBT are shown in Figure 5-3(a). The transconductance g_m for the dual-cell devices was nominally 85 to 95 mS measured at 50% of the zero-bias saturation current I_{ces}. The nominal value of I_{ces} was 90 mA. The base-to-collector reverse breakdown voltage was typically 17 to 18 V for the dual-cell PBT. Mapping of the dc characteristics has indicated fairly good uniformity over a wafer. For instance, when looking at g_m on one particular wafer, 2BB69, 50% of all of the devices were within the range of 80 to 95 mS.

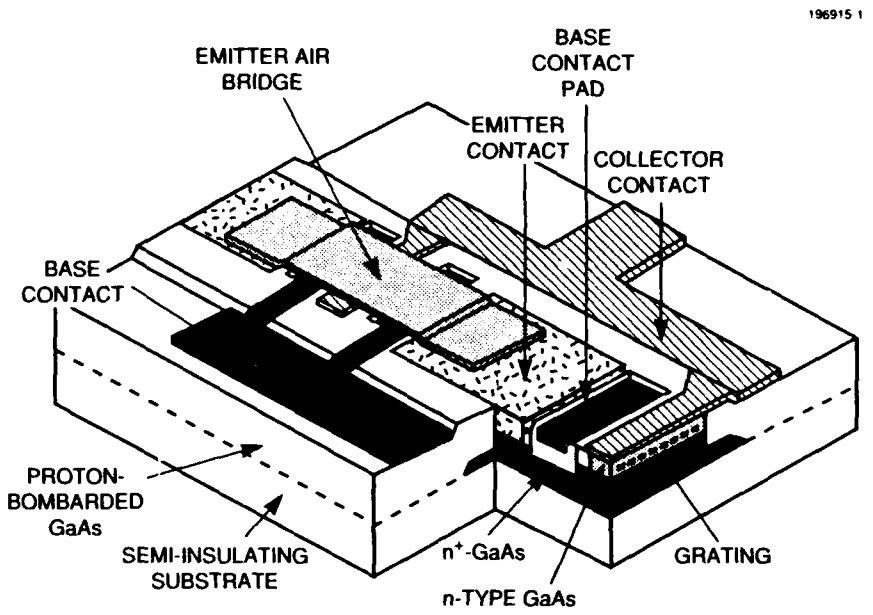

Figure 5-1. Cutaway schematic of a dual-cell GaAs PBT.

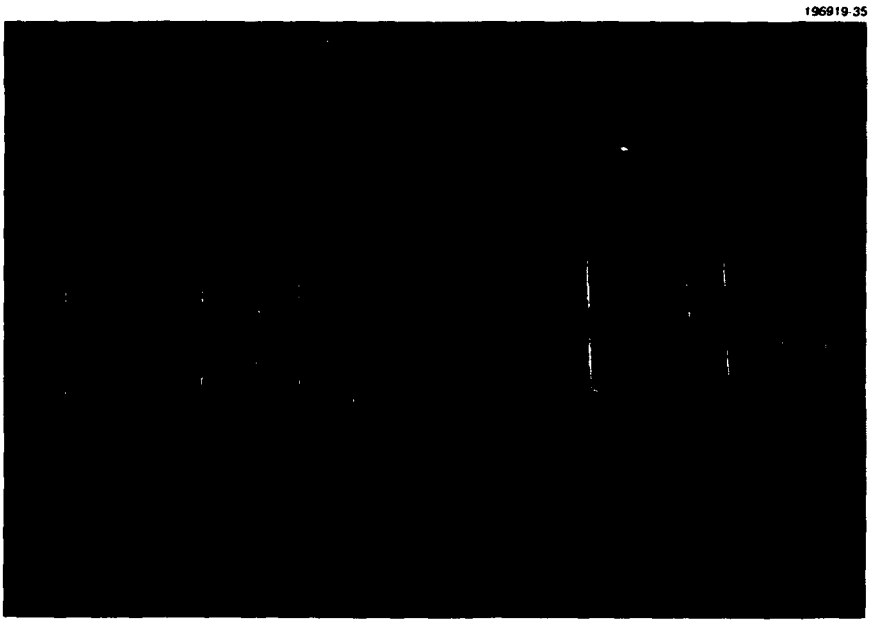

Figure 5-2. Scanning electron micrograph of a four-cell PBT.

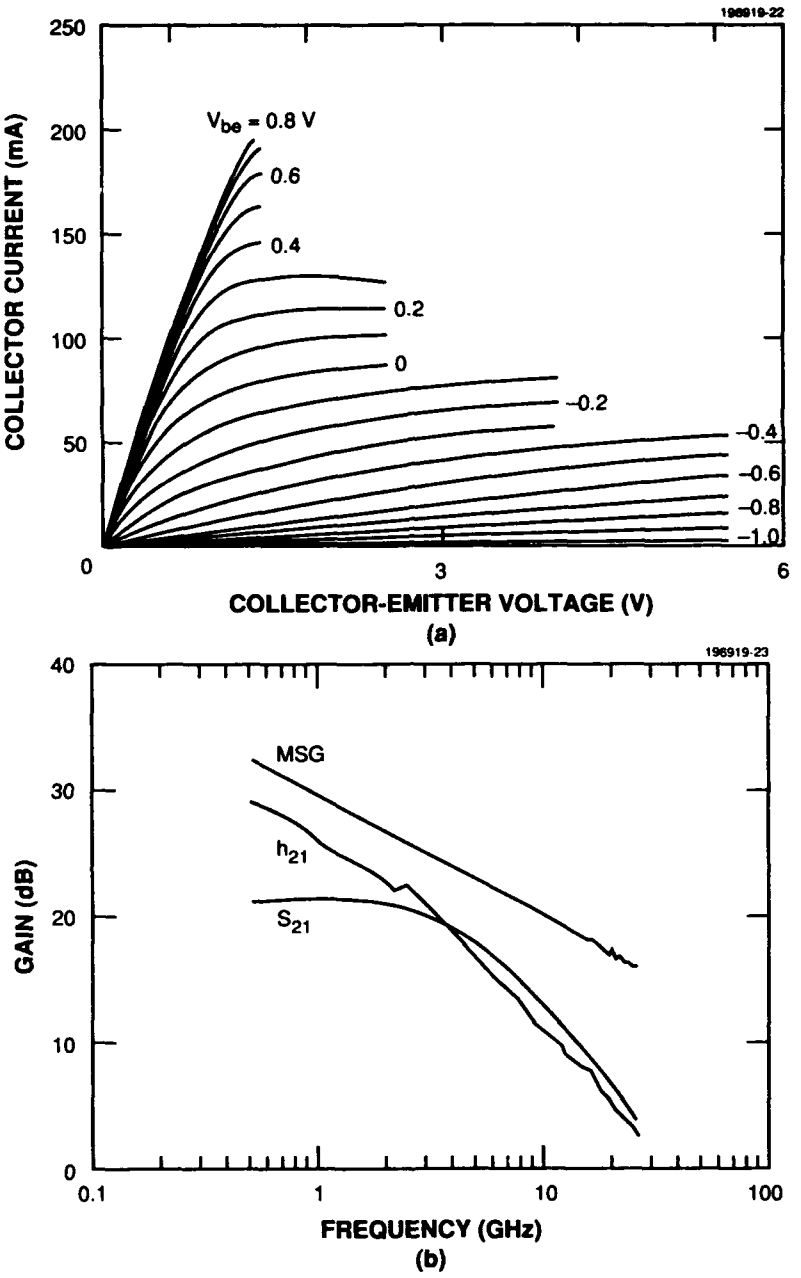

Figure 5-3. Measured dual-cell PBT characteristics. (a) Collector current vs collector-emitter voltage for base voltage from −1.0 to 0.8 V. (b) Small signal transducer gain S_{21}, maximum stable gain (MSG), and current gain h_{21} vs frequency.

The small signal transducer gain S_{21}, the maximum stable gain (MSG), and the current gain h_{21} vs frequency for the dual-cell PBT obtained from on-wafer measurements are shown in Figure 5-3(b). The small signal gain was nearly identical to that measured for single-cell PBTs from the same wafer. The dc and small signal parameters of these PBTs scaled as a function of the number of active cells n (e.g., the device impedance

scaled as $1/n$, and current and g_m scaled directly with n). The nominal unity-current-gain frequency for dual-cell devices is 35 GHz. The reverse isolation S_{12} was measured to be < −25 dB at 21 GHz. The power performance of these devices is reported in the next section.

K. B. Nichols R. G. Drangmeister
R. Actis R. A. McMorran
C. L. Dennis A. Vera
D. J. Baker R. W. Chick

5.2 20-GHz HIGH-EFFICIENCY POWER AMPLIFIERS USING MONOLITHIC MULTICELL PBTs

The dual-cell and four-cell PBTs described in Section 5.1 have been used to construct several 20-GHz power amplifiers. In the first step of this process, computer-aided active load-pull measurements [5],[6] were performed over the range from 19.7 to 21.7 GHz to evaluate the optimum power-added efficiency, output power, and gain of the PBTs as a function of device bias, drive level, and frequency. The measurement system software provided direct control of the latter parameters with real-time display of device efficiency, output power, and embedding impedances. For these measurements, the devices were individually separated from the wafer and mounted into 254-μm-thick alumina microstrip circuits using 5.08-μm-thick photolithographically produced bonding ribbons. Other details of the packaging of these devices are described in [7]. In some cases, the results were obtained using input prematching circuits in order to minimize measurement error sensitivity and to maximize the incident power from sources with limited output power capability.

Table 5-1 summarizes the measured load-pull results for the dual-cell and four-cell PBTs from two wafers. The dual-cell devices typically demonstrated ~250-mW capability, with a high of 334 mW obtained for the 2BB58

TABLE 5-1

Summary of Best and Typical Results of Load-Pull Device Characterizations for Dual-Cell and Four-Cell GaAs PBTs

Wafer	Device Type	Case	Output Power (mW)	Gain (dB)	DC Power (mW)	Power-Added Efficiency (%)	Frequency (GHz)
2BB69	Dual-cell	Best	287	5.6	509	41	20.7
2BB69	Dual-cell	Typical	246	5.9	457	40	20.7
2BB58	Dual-cell	Best	334	5.3	532	44	20.7
2BB58	Dual-cell	Typical	302	5.8	542	41	20.7
2BB69	Four-cell	Best	653	6.2	1200	42	20.2
2BB69	Four-cell	Typical	436	5.3	960	35	20.7
2BB58	Four-cell	Typical	510	5.7	981	38	20.7

wafer. The power-added efficiencies were all 40% or above with a best of 44%, while the gains for all of the dual-cell PBTs were in the range of 5.3 to 5.9 dB. The minimum power capability for the four-cell devices was ~ 430 mW, with a maximum of 653 mW from the 2BB69 wafer. The power-added efficiencies were all 35% or above with a best of 42%, while the gains for all of the four-cell PBTs were in the range of 5.3 to 6.2 dB.

The impedance data determined from the load-pull measurements were used in the next step to design impedance matching networks for several microstrip amplifiers employing dual-cell and four-cell PBTs. These amplifiers were then fabricated and tested. Their performance is summarized in Table 5-2, which includes all circuit and connector losses.

TABLE 5-2

Typical Connectorized Multicell PBT Amplifier Performance

Frequency (GHz)	Number of Dual-Cell Devices	Number of Four-Cell Devices	Gain (dB)	Output Power (mW)	Power-Added Efficiency (%)	DC Power (W)
20.7	0	3	9.2	667	25	2.34
20.7	1	1	9.5	417	31	1.23
20.5	0	1	5.57	437	35	0.89
20.5	0	2	4.44	700	26	1.696
20.5	1	0	5.79	240	37	0.47

A two-stage microstrip PBT amplifier is shown in Figure 5-4. This amplifier produced 430 mW of output power with 33% power-added efficiency with the connector losses removed. The two-stage design utilizes a dual-cell device to drive a four-cell PBT. A coupled-line dc-blocking capacitor provides the bias isolation between the two stages. On-board oscillation suppression circuits that use thin-film resistors in series with beam-lead capacitors are employed to eliminate undesired lower-frequency instabilities. The output power, gain, and power-added efficiency of this amplifier at 20.7 GHz are shown in Figure 5-5. The coaxial connectors of the amplifier each contribute 0.2 dB of loss, which is removed from the data of the figure.

Several amplifiers using these new multicell power PBTs have been constructed and measured in order to evaluate the PBT performance in actual circuits. Including connector losses, an output power of 667 mW with 9.2 dB of gain and 25.1% power-added efficiency at 20.7 GHz was demonstrated in a microstrip amplifier incorporating three four-cell PBTs. The availability of PBTs capable of output powers above 400 mW makes it possible to utilize them in low-loss power-combining circuits to achieve several watts of output power with overall efficiencies approaching 30%.

R. Actis
R. W. Chick
K. B. Nichols
R. A. McMorran

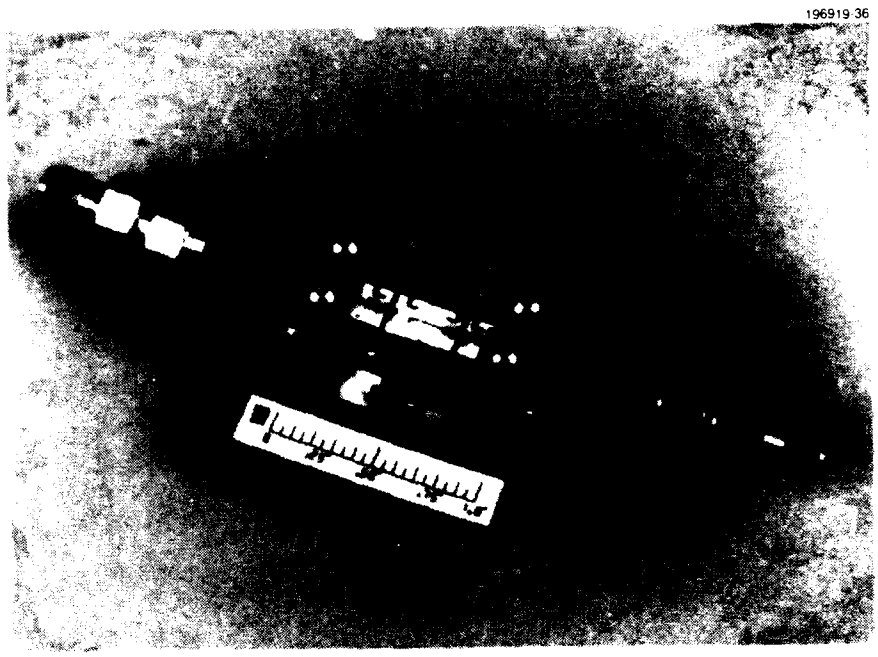

Figure 5-4. Two-stage microstrip PBT amplifier fabricated on 254-μm alumina microstrip substrate.

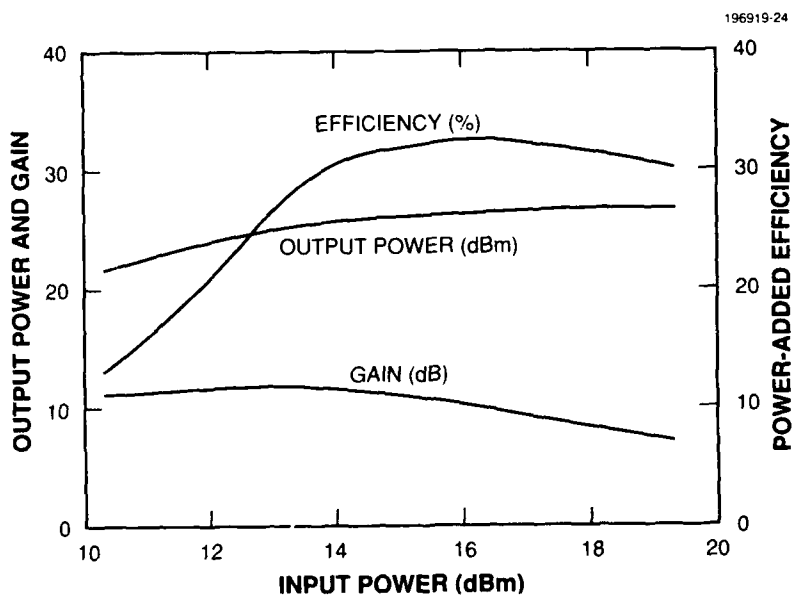

Figure 5-5. Output power, gain, and power-added efficiency as a function of input drive level for a two-stage PBT amplifier. The measurement frequency is 20.7 GHz and the connector losses are removed.

REFERENCES

1. L. J. Kushner, M. A. Hollis, R. H. Mathews, K. B. Nichols, and C. O. Bozler, *Dig. Tech. Papers, IEEE MTT-S Int. Microwave Symp.* (IEEE, New York, 1988), Vol. 1, p. 525.

2. K. B. Nichols, M. A. Hollis, C. O. Bozler, M. A. Quddus, L. J. Kushner, R. H. Mathews, A. Vera, S. Rabe, R. A. Murphy, and D. L. Olsson, *Proc. IEEE/Cornell Conf. on Advanced Concepts in High Speed Semiconductor Devices and Circuits* (IEEE, New York, 1987), p. 307.

3. R. A. Murphy and J. D. Murphy, *Microwave J.* **30**(7), 101 (1987).

4. K. B. Nichols, R. Actis, C. L. Dennis, D. J. Baker, B. F. Gramstorff, R. G. Drangmeister, A. Vera, and R. W. Chick, submitted to *IEEE Electron Device Lett.*

5. R. Actis and R. A. McMorran, *Appl. Microwave Mag.* **1**(3), 91 (1989).

6. R. S. Tucker and P. D. Bradley, *IEEE Trans. Microwave Theory Tech.* **MTT-32**, 296 (1984).

7. R. Actis, K. B. Nichols, R. W. Chick, and R. A. McMorran, presented at 1992 IEEE MTT-S Int. Microwave Symp., Albuquerque, N.M., 1-5 June 1992.

6. MICROELECTRONICS

6.1 ARCHITECTURE AND ACCURACY ANALYSIS OF A CCD FFT PROCESSOR

The architecture of a charge-coupled device (CCD) radix-4 fast Fourier transform (FFT) processor is described here, and the results of an accuracy analysis of the processor are presented. The term FFT refers to one of a family of algorithms for computing the discrete Fourier transform (DFT), a fundamental discrete-time signal processing tool [1]. The most commonly used Cooley-Tukey FFT algorithms reduce the computational cost of an N-sample point DFT from $O(N^2)$ to $O(N\log N)$ operations through an index remapping scheme. Suppose that N is a composite number such that $N = R^k$ where R is called the radix. Then the DFT of an original N-point sequence can be computed by performing kR^2 R-point DFTs along with a number of auxiliary multiplications by constants called twiddle factors. This scheme is referred to as an N-point radix-R FFT and results in considerable computation savings when N is large. The index remapping for a one-dimensional sequence of length $N = R^k$ is best visualized as the process of writing ("warping") the original sequence into a k-dimensional array with sides of length R. The FFT is then performed by computing short DFTs each of length R along every dimension of the warped array, with twiddle multiplications interleaved between sets of DFTs. For example, a 64-point sequence can be written into a $4 \times 4 \times 4$ array. A radix-4 FFT of this sequence consists of 16 four-point DFTs in the x-direction, twiddle multiplications, 16 DFTs in the y-direction, twiddles, and finally 16 DFTs in the z-direction.

Selecting the appropriate samples for each R-point DFT from the warped sequence is a nontrivial addressing problem when the samples in reality are stored sequentially in computer memory. The proposed CCD architecture eliminates the typical need for a complex address-generating scheme by storing and shifting the sequence in and through a collection of serial and parallel shift registers. The order of reads from and writes to the registers is extremely regular, yet the "corner-turning" of the warped sequence is achieved without overhead computation for address generation.

A block diagram of the CCD radix-4 FFT architecture is shown in Figure 6-1. The 4-point DFTs are computed by the four vector-matrix product (VMP) sections [2] shown in the bottom left of the figure, while twiddle multiplications are performed by the four multiplying digital-to-analog converters (MDACs) [3]. The operation of the CCD FFT processor is as follows. The real components of a complex input sequence $x[n]$ are loaded into the shift registers b_0 through b_3, while the corresponding imaginary parts are loaded into d_0 through d_3. The real parts of samples $x[0], x[4], x[8], \ldots$ are placed in b_0; real parts of samples $x[1], x[5], x[9], \ldots$ are assigned to b_1, and so forth. Samples are read from b_0 and d_0 in sets of four, multiplied by appropriate twiddle factors, and broadcast down the vertical lines in the VMP structure. The samples are weighted by the values shown in the squares, summed along the horizontal lines, and written into registers a_0 through a_3 and c_0 through c_3. After all samples have been read from registers b_0 and d_0, samples are read from b_1 and d_1. The process continues until the last samples from b_3 and d_3 have been processed and written into a_3 and c_3. At this point the 4-point DFTs through the first dimension of the warped sequence have been performed. The data are then transferred in parallel from the a and c registers back to the b and d registers, respectively. The parallel transfer completes the corner-turning of the array. For an $N = 4^k$-point DFT this process is repeated k times, after which the transformed sequence appears in the a and c registers.

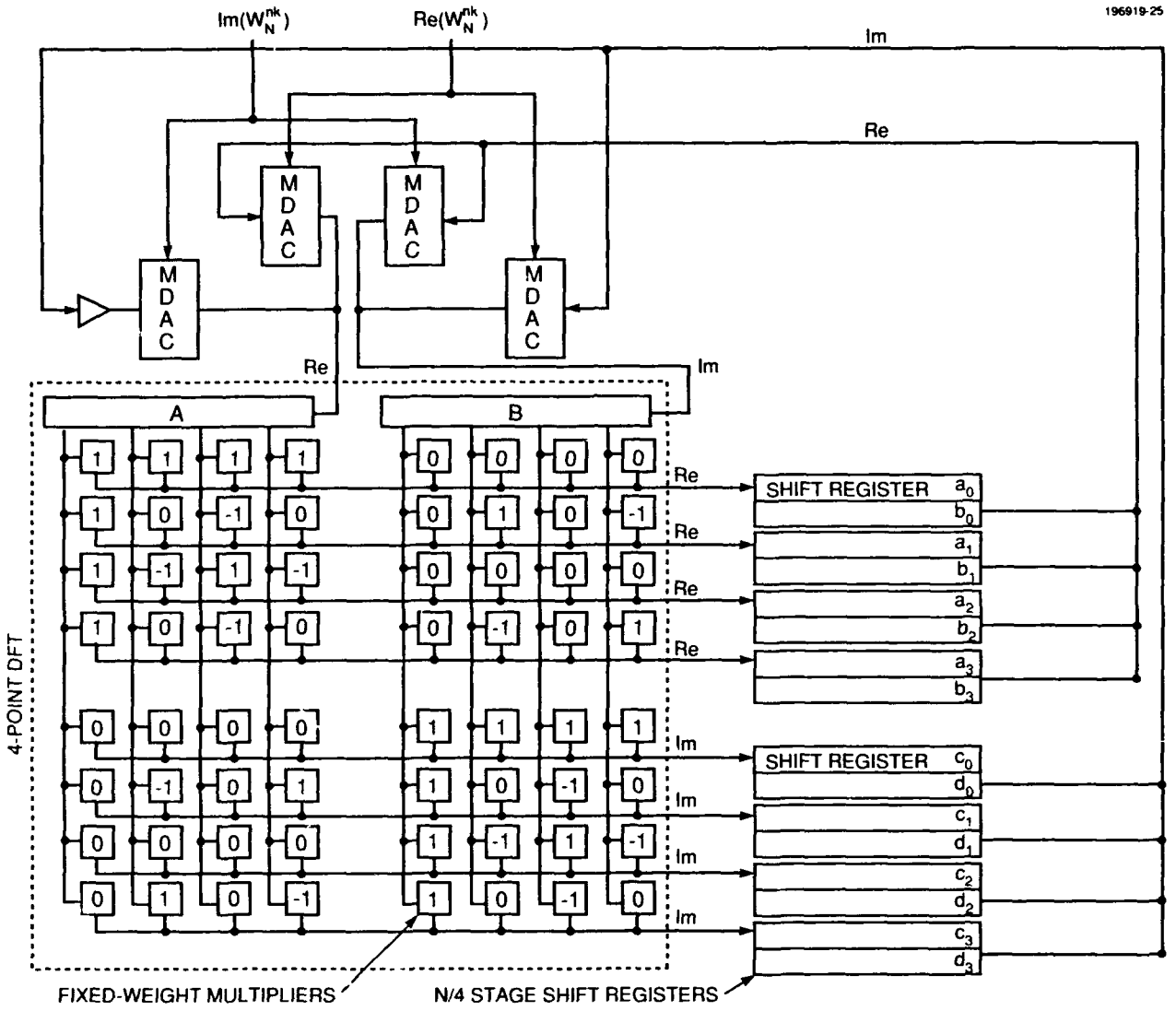

Figure 6-1. Block diagram of the proposed CCD FFT radix-4 architecture.

Several CCD FFT processors can be pipelined for greater throughput. At a 10-MHz clock rate a single CCD FFT processor can compute a 1024-point complex radix-4 FFT in 102 μs. Five pipelined processors can be pipelined to produce a 1024-point transform every 20.5 μs.

Both a computer simulation and a mathematical analysis of the output accuracy of the CCD FFT processor have been performed. The accuracy is determined by a combination of the number of bits in each word of twiddle-factor memory and the accuracy of the MDACs. The analysis used the standard error model in which the effects of both twiddle-factor truncation and finite-accuracy computation are described as additive uncorrelated white noise. Although the modeling of truncation error as probabilistic is clearly

incorrect (once a twiddle-factor representation is selected the error is known and fixed), in practice the model is quite accurate. The results of the simulations agree well with the analysis and indicate that for MDACs with 8-bit twiddle words, 8 bits of computation accuracy yield a 1024-point FFT with 36-dB (~ 6 bits) accuracy. Nine and 12 bits of computation accuracy give output accuracies of 42 dB (~ 7 bits) and 52 dB (between 8 and 9 bits), respectively.

A. M. Chiang
M. L. Chuang

REFERENCES

1. C. S. Burrus, in *Advanced Topics in Signal Processing*, J. S. Lim and A. V. Oppenheim, eds. (Prentice-Hall, Englewood Cliffs, N.J., 1988).

2. A. M. Chiang, *Proc. SPIE* **845**, 2 (1987).

3. A. M. Chiang, *IEEE J. Solid-State Circuits* **25**, 1510 (1990).

7. ANALOG DEVICE TECHNOLOGY

7.1 DUAL-CHANNEL, 512-SAMPLE, 256-TAP ANALOG-TERNARY CMOS/CCD CORRELATOR

A charge-coupled device (CCD) dual-correlator chip was designed and subsequently fabricated at a commercial foundry using a custom 2-μm CMOS process. A photomicrograph of the chip is shown in Figure 7-1, and its specifications are provided in Table 7-1. Each of the two identical subunits within the device correlates a sampled analog input signal with a programmable binary reference, producing a sampled analog output correlation. Other than sharing common power and ground connections, the two correlators are totally independent of one another and can therefore be individually programmed. This is advantageous for applications requiring the simultaneous processing of in-phase and quadrature signal components.

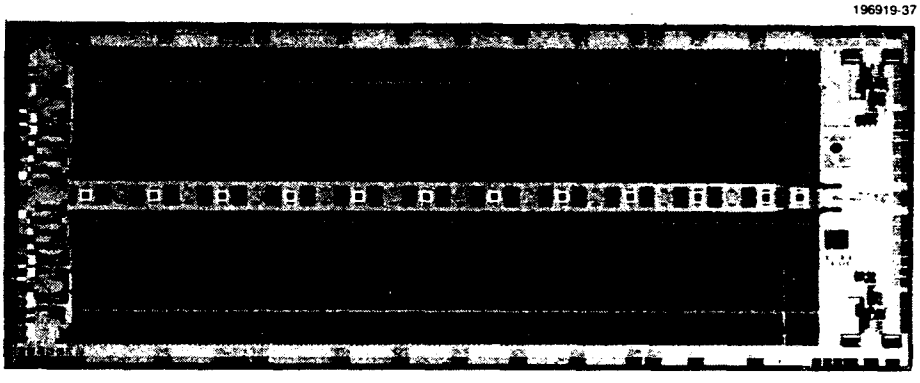

Figure 7-1. Photomicrograph of a dual-channel, 512-sample, 256-tap analog-ternary CMOS/CCD correlator. The chip size is 14.5 ×5.6 mm.

Each correlator principally consists of a 512-sample CCD delay line tapped every other stage for a total of 256 taps. An additional short, 24-sample, 12-tap correlator section is appended to the end of each correlator. These short sections can be isolated from their long preceding sections when better short-code high-frequency performance is required. Taps are programmed in a ternary fashion to a plus, minus, or zero weight so that the correlators are ideally suited to the matched filtering of binary-coded communication signals. The plus or minus state of each tap is programmed by loading a reference code into each correlator, while a separate mask word is used to determine which taps are turned off for zero weight. Zero tap weighting allows the correlator length to be adjusted to that of incoming codes. Input signals can be sampled at a rate ranging from kilosamples per second to a high of 50 megasamples per second (Msps).

Because of the amount of circuitry required to program each correlator and the requisite large number of transistors, CMOS technology has been employed to keep overall power dissipation below 1 W. The circuit density as well as CCD pitch are such that only every other stage of the CCD can be effectively tapped, so that every other sample resident within the CCD at any time contributes to a correlator's output. One consequence

of this arrangement is that each correlator is capable of processing two signals at the same time. Independent interleaved correlations are produced at the output as a result of alternately sampling two signals at the input. A single signal, on the other hand, must be double sampled. Under these conditions, the two resultant interleaved correlations at the output will be identical so long as input samples never occur during code bit transitions. This characteristic can, therefore, be exploited for the fine tuning of sample-clock timing.

TABLE 7-1

Specifications of CMOS/CCD Correlator

Dual 512-sample, 256-tap architecture
Reference code weights: +1, 0, –1
Maximum sample rate: 50 Msps
Minimum (noise-limited) dynamic range at 50 Msps: 54 dB
Total harmonic distortion (for < 10 Msps): < –40 dB
Electrical length: 2 to 256 taps
Power dissipation: < 1 W
On-chip CCD clock drivers and 50-Ω output drivers
On-chip static protection
Ground-centered inputs and outputs
User-friendly device programming interface
5-V CMOS and TTL logic compatibility
69-lead pin-grid-array custom-designed package

Figure 7-2 shows the autocorrelation of 255-chip *m*-sequences on different scales and at different rates. Figure 7-2(a) was obtained by wafer probes at a sample rate of 0.1 Msps. The top trace is the input code for this case, and the bottom trace shows the resultant output correlation. Figures 7-2(b) and 7-2(c) are the correlations obtained at 5 and 25 Msps, respectively, using packaged devices. Since the the *m*-sequences are continuous, the sidelobes under ideal conditions should be perfectly flat.

A number of features have been incorporated to ease the burden of interfacing to the chip. On the analog side, inputs and outputs were designed for ground-centered signals, eliminating the need to deal with offsets. The digital programming interface, on the other hand, was designed to minimize signal-to-signal timing problems while simultaneously maximizing overall programming flexibility. In this regard, all digital inputs can be clocked concurrently from a common latch with clock enables allowing for the use of free running clocks, and clock and strobe functions are fully edge triggered so that they complete their tasks soon after a rising edge. Furthermore, the reference (plus or minus) code and mask word can be independently loaded and held without affecting the current state of the taps. These stored patterns can then be activated at any time by the application of an updating strobe pulse. For added flexibility, all digital inputs are both CMOS and TTL compatible, while the integral output drivers have been provided with the capability to drive 50-Ω loads, since

these are often encountered in receiver applications. Finally, the entire chip has been designed to operate from standard ± 5-V supplies.

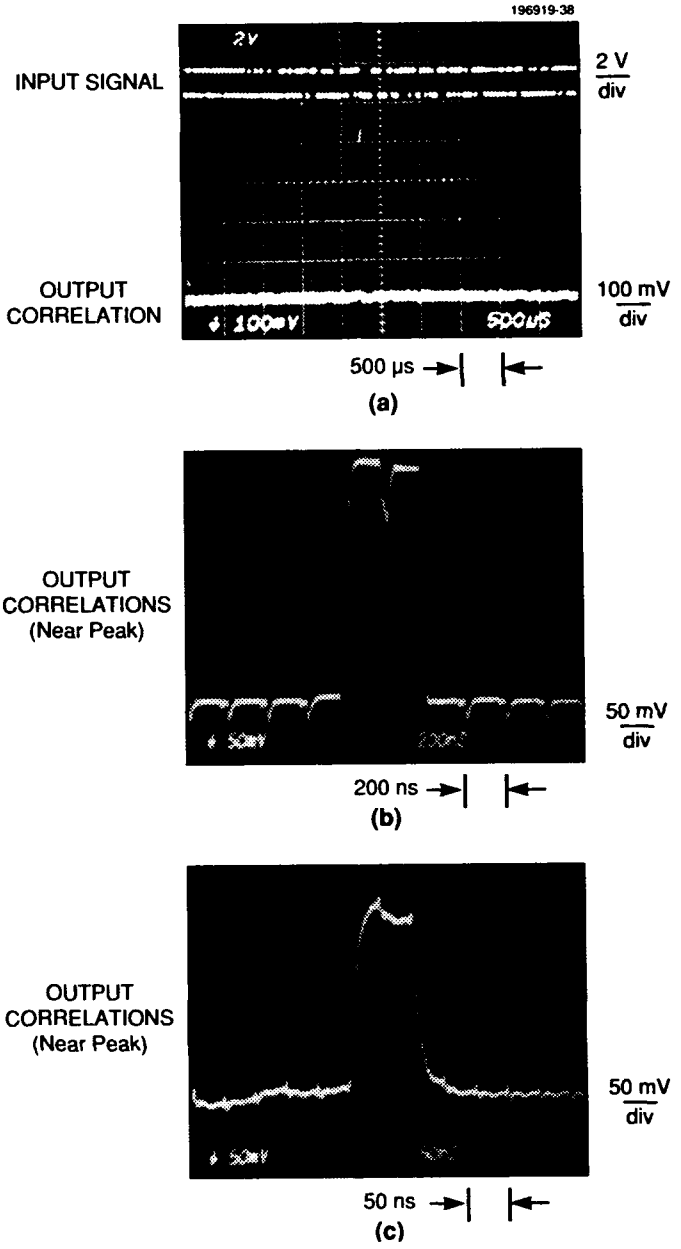

Figure 7-2. Performance of the correlator in processing 255-chip m-sequences. Correlations were obtained (a) by wafer probes at 0.1 Msps and (b),(c) by using package devices at 5 and 25 Msps, respectively.

A 69-lead pin-grid-array ceramic package has been custom designed for the chip. The package possesses multiple bonding-pad tiers with internal power and ground planes that minimize the required number of package pins while providing significant shielding for internal signal traces. Such a structure is expected to provide superior high-frequency performance over that provided by standard nonshielded package configurations.

Overall performance of the chip has exceeded expectations for a first-run chip of this size and complexity. Changes to reduce nonlinearities and to extend both the dynamic range and the maximum sampling rate will be incorporated into the next design.

D. R. Arsenault

7.2 GAS CONDUCTION HEATER

Substrate temperature during deposition is one of the most important parameters defining the microstructure and electronic properties of thin films. Yet, its measurement and control, in the low-pressure ambient characteristic of most thin-film deposition processes, is a problem that has so far eluded a simple universal solution. In most deposition systems the substrate is mounted on a flat metal plate whose temperature can be accurately monitored. However, at pressures in the range of tens of millitorr the thermal contact between the substrate and plate is poor, owing to their roughness and nonflatness. Even for temperatures in the 100°C range, heat transfer occurs mainly by radiation [1]. Because many substrates of technological interest are transparent in the near infrared, and because during film deposition the optical constants of the substrate-film composite change continuously, the measurement and control of the substrate temperature become extremely difficult, and errors in the range of hundreds of degrees in the reported temperature are not uncommon [2].

A number of solutions to this problem have been proposed. One approach is to enhance the thermal contact between the substrate and the heater plate, most frequently by soft metal [3] or molten metal [4] interfaces or one of a variety of "gluing" methods [5],[6]. In the latter techniques, a paste of fine metal particles dispersed in a binder, which is burned off, is used to fix the substrate to the holder. These methods are cumbersome and in many cases introduce contamination to the process and prevent films from being deposited on both sides of the wafer.

Another approach is to radiatively heat the substrate while using remote measurement for control of the substrate temperature [7]. In this case, pyrometers are usually employed to measure the substrate temperature. However, the rapid variation of the optical properties of the substrate and film dictates the use of sophisticated adaptive techniques, requiring knowledge of the infrared properties of the substrate and film [8], which are often unknown.

A more elegant and less cumbersome solution to the substrate heating problem is to create a pocket of gas behind the wafer with pressure high enough to ensure good thermal contact to the heater block. A simple calculation shows that for a thin layer of gas of the order of the mean free path and a substrate temperature around 800°C, a temperature drop of only 10 to 40°C is expected between the heater and the substrate. The exact amount of this decrease depends on the efficiency of the thermal transfer between the gas and the

substrate and heater [9]. Because the drop is small, changes in substrate emissivity during film deposition result in only small changes in the substrate temperature.

We have implemented two heater designs based on this idea. A simple implementation that we used to establish the feasibility of the approach is shown in Figure 7-3. A cylinder was machined of 316 stainless steel with a 6.4-cm diameter and a 3.8-cm height, and one of its plane surfaces was lapped flat. The cylinder was then annealed in vacuum to 800°C to eliminate thermal stresses and lapped and polished to better than two wavelengths over the surface. A sealing ring of oxidation-resistant Haynes alloy 230 with an o.d. of 5.2 cm, an i.d. of 4.8 cm, and a height of 2 μm was then deposited by sputtering, using a metal mask. A weighted annular plate was employed to apply pressure to a 5-cm-diam wafer immediately above the sealing ring, as shown in Figure 7-3. The weight was chosen such that gas pressures up to 40 Torr could be applied behind the wafer. Gas was introduced through a series of holes connecting to a high-conductance channel inside the heater. The sizes of the holes and the channel were calculated such that the expected gas leaks through the seal, due to nonflatness of the wafer and heater, would have negligible effect on the gas pressure uniformity behind the substrate. In this simple implementation, the stainless steel block was heated by two commercially available cartridge heaters. A thermocouple was placed in a well near the cartridges.

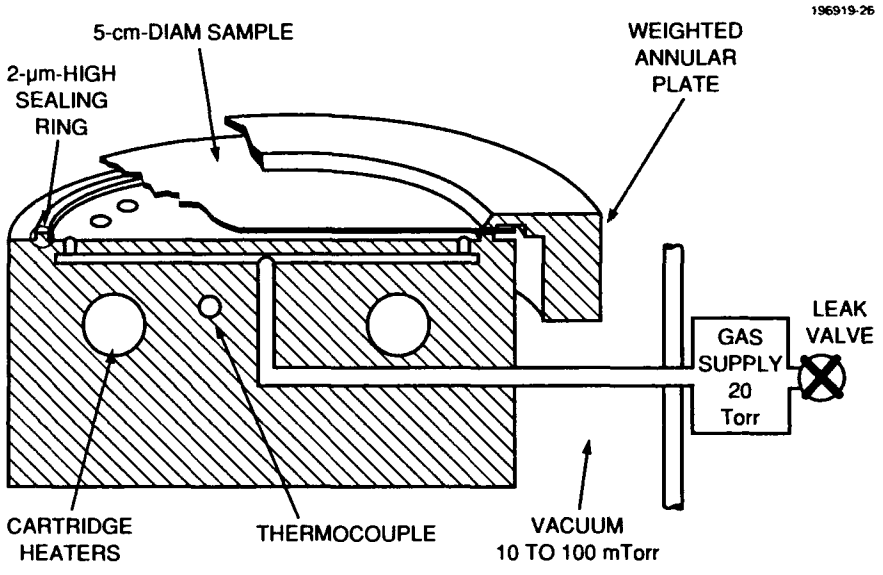

Figure 7-3. Cross section of the gas conduction heater with the wafer in place.

The effect of adding helium, argon, or oxygen behind the substrate is shown in Figure 7-4. The substrate temperature was determined by a 25-μm-diam wire thermocouple attached to the substrate surface using a process previously developed in our laboratory [5]. During these measurements the heater block temperature near the thermocouple was maintained at 740°C. The figure shows that the temperature of the substrate rises from 380 to 680°C when the pressure is raised from 0 to 30 Torr. Little difference is seen between the gases.

The higher heating transfer due to the low mass of helium is offset by a lower efficiency of heat transfer between the helium and the heater and substrate surfaces. For pressures > 20 Torr the substrate temperature is only a weak function of gas pressure, so pressure control is not critical.

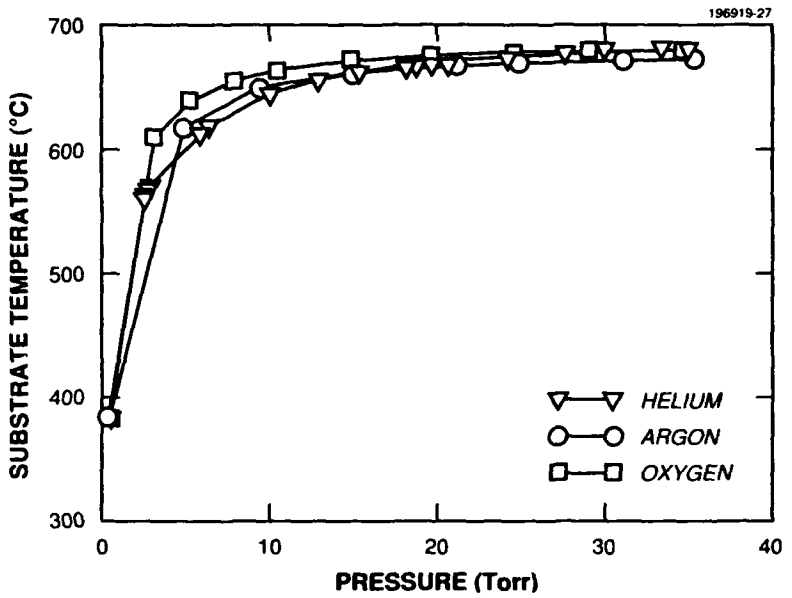

Figure 7-4. Variation of the surface temperature of a $LaAlO_3$ wafer with gas pressure in the volume behind the substrate. The temperature of the heater immediately below the substrate is estimated to be 710°C.

Figure 7-5 shows the difference in temperature between two points on the substrate surface, one in the center of the substrate and the other near the clamping ring that applies pressure to the substrate. Oxygen was used for these measurements. The maximum temperature difference is < 1°C for substrate temperature in the range of 680 to 720°C. These are the temperatures of interest for deposition of good, high-T_c superconductive oxide films. The gas flow necessary to keep 30 Torr behind the wafer during the measurements was $< 5 \times 10^{-1}$ sccm.

A second version of the gas conduction heater using springs instead of a weight to press the substrate against the sealing ring was also built. This version was used in a sputtering system, where the substrate and target are positioned vertically, to deposit uniform YBCO films onto a 700°C, 5-cm-diam $LaAlO_3$ substrate. Use of this gas conduction heater, with oxygen as a conduction medium, should allow deposition of films on both sides of the wafer. Films of YBCO are unstable at high temperature in the absence of oxygen. Calculations based on measured elastic properties of $LaAlO_3$ indicate that the extension of the method to 7.5-cm-diam substrates is feasible.

A. C. Anderson
R. S. Slattery
A. C. Westerheim

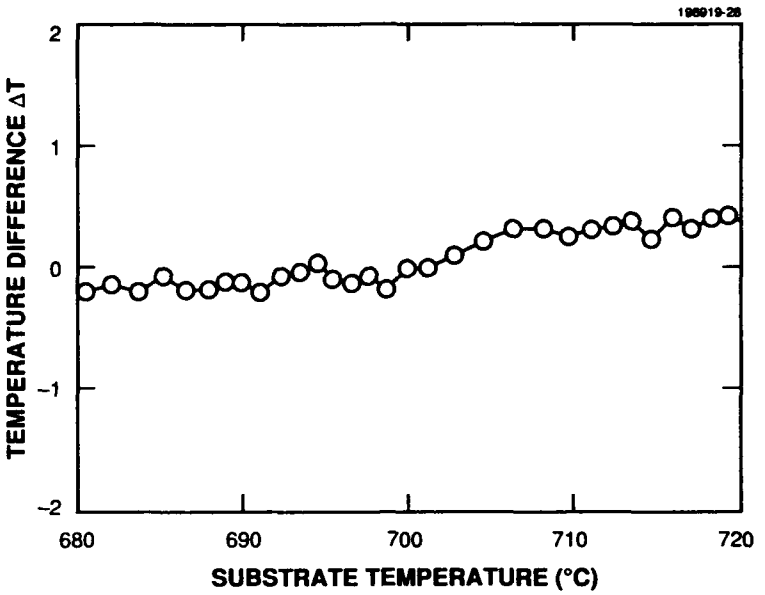

Figure 7-5. Difference between the temperature at the center of the substrate and in a position 6 mm from the clamping ring as a function of the temperature at the center.

REFERENCES

1. M. G. Copper, B. B. Mikic, and M. M. Yovanovich, *Int. J. Heat Mass Transfer* **12**, 279 (1969).
2. S. Witanachchi, H. S. Kwok, X. W. Wang, and D. T. Shaw, *Appl. Phys. Lett.* **53**, 234 (1988).
3. R. G. Humphreys, J. S. Satchell, N. G. Chew, J. A. Edwards, S. W. Goodyear, S. E. Blenkinsop, O. D. Dosser, and A. G. Cullis, *Supercond. Sci. Technol.* **3**, 38 (1990).
4. G. J. Davies and D. Williams, in *The Technology and Physics of Molecular Beam Epitaxy*, E. H. C. Parker, ed. (Plenum, New York, 1985), p. 22.
5. A. C. Westerheim, A. C. Anderson, and M. J. Cima, *Rev. Sci. Instrum.* **63**, 2282 (1992).
6. S. R. Foltyn, R. E. Muenchausen, R. C. Dye, X. D. Wu, L. Luo, D. W. Cooke, and R. C. Taber, Los Alamos National Laboratory, Report LA-UR-91-308 ERDC, 1991.
7. D. E. Mars and J. N. Miller, *J. Vac. Sci. Technol. B* **4**, 571 (1986).
8. B. I. Choi, A. C. Anderson, A. C. Westerheim, M. I. Flik, and Z. M. Zhang, presented at the Fall Mtg. Materials Research Soc., Boston, Mass., 2-6 December 1991.
9. F. M. Devienne, in *Advances in Heat Transfer*, J. P. Hartnett and T. F. Irvine, Jr., eds., Vol. 2 (Academic, New York, 1965), p. 271.

REPORT DOCUMENTATION PAGE

Form Approved
OMB No. 0704-0188

1. AGENCY USE ONLY (*Leave blank*)	2. REPORT DATE	3. REPORT TYPE AND DATES COVERED
	15 February 1992	Quarterly Technical Report, 1 November 1991 - 31 January 1992

4. TITLE AND SUBTITLE

Solid State Research

5. FUNDING NUMBERS

C — F19628-90-C-0002
PE — 63250F
PR — 221

6. AUTHOR(S)

Alan L. McWhorter

7. PERFORMING ORGANIZATION NAME(S) AND ADDRESS(ES)

Lincoln Laboratory, MIT
P.O. Box 73
Lexington, MA 02173-9108

8. PERFORMING ORGANIZATION REPORT NUMBER

1992:1

9. SPONSORING/MONITORING AGENCY NAME(S) AND ADDRESS(ES)

HQ AF Materiel Command, USAF
Wright-Patterson AFB, OH 45433-5001

10. SPONSORING/MONITORING AGENCY REPORT NUMBER

ESC-TR-92-075

11. SUPPLEMENTARY NOTES

None

12a. DISTRIBUTION/AVAILABILITY STATEMENT

Approved for public release; distribution is unlimited.

12b. DISTRIBUTION CODE

13. ABSTRACT (*Maximum 200 words*)

This report covers in detail the research work of the Solid State Division at Lincoln Laboratory for the period 1 November 1991 through 31 January 1992. The topics covered are Electrooptical Devices, Quantum Electronics, Materials Research, Submicrometer Technology, High Speed Electronics, Microelectronics, and Analog Device Technology. Funding is provided primarily by the Air Force, with additional support provided by the Army, DARPA, Navy, SDIO, NASA, and DOE.

14. SUBJECT TERMS

electrooptical devices	high-speed electronics	optical modulators	selective-area growth
quantum electronics	microelectronics	microlenses	microwave semiconductor devices
materials research	analog device technology	infrared detector arrays	charge-coupled devices
submicrometer technology	lasers	surface-emitting lasers	deposition-temperature control

15. NUMBER OF PAGES
86

16. PRICE CODE

17. SECURITY CLASSIFICATION OF REPORT	18. SECURITY CLASSIFICATION OF THIS PAGE	19. SECURITY CLASSIFICATION OF ABSTRACT	20. LIMITATION OF ABSTRACT
Unclassified	Unclassified	SAR	